IPP-Report

Max-Planck-Institut
für Plasmaphysik

P. Bachmann, J. Kisslinger, D. Sünder, H. Wobig

Bifurcation of Temperature in the Boundary Region of Advanced Stellarators

IPP III/262

Mai 2000

Bifurcation of Temperature in the Boundary Region of Advanced Stellarators

P. Bachmann*, J. Kisslinger, D. Sünder*, H. Wobig

Max-Planck-Institut für Plasmaphysik, Garching bei München, EURATOM-Ass.
* Bereich Plasmadiagnostik Berlin

Abstract:

The following paper discusses some problems of the island divertor in the Wendelstein 7-X configuration and the Helias reactor (HSR) configuration. These islands exist on the $\iota = 1$-surface at the plasma boundary and will be utilised for impurity control in the Wendelstein 7-X experiment. The structure of this island region depends on the plasma pressure and the tendency is to become more and more ergodic with rising plasma pressure. Thermal transport in the divertor region is described by the transport equation, which is inherently three-dimensional. By averaging along the helical geometry of the island this equation can be reduced to a two-dimensional one describing the temperature distribution on the poloidal plane. In this approximation there is a strong similarity to tokamak geometry. Since the islands are modified by the plasma currents a finite beta equilibrium is computed as the starting point for the geometric analysis of divertor action. Anomalous transport strongly affects the width of the scrape-off layer and the width of the wetted area on the divertor target plates. The nonlinearity of the radiation losses in the divertor region and the non-linearity of the boundary conditions can lead to a bifurcation of the temperature distribution and to multiple solutions. Some numerical examples of temperature profiles and bifurcated solutions are given. In the appendix the basic bifurcation phenomena are studied by using phase space analysis.

1. Introduction

In the boundary region of stellarators magnetic surfaces, in general, do not exist. The last magnetic surface is surrounded by magnetic islands and stochastic regions. Field lines can be closed or cover a bounded region ergodically and several field lines are intersecting first wall or divertor target plates. The temperature distribution in this region is the result of cross-field thermal conduction and parallel heat conduction. Furthermore, the radiation by impurities plays a large role in determining the temperature profile. It is well known that the non-linear temperature dependence of the radiation function is the reason for bifurcation of the temperature profile and local radiation maxima, called MARFEs. Another cause of bifurcation is the non-linear relation between temperature and temperature gradients at the divertor target plates originating from the physics processes close to the target plates. These issues have been extensively studied in tokamak plasma, where axissymmetry reduces the analysis to two-dimensional problems [1,2,3,4,5]. Some mathematical issues of the 3–D heat conduction equation have been investigated in [6].

The Wendelstein 7-X configuration is an advanced stellarator with reduced Pfirsch-Schlüter currents [7]. The rotational transform is 0.84 in the plasma center and close to one at the plasma edge. There are 5 magnetic islands at the plasma boundary, which are scheduled to serve as divertor geometry. For this purpose target plates will be installed at the backside of the islands and after crossing the last closed magnetic surface the plasma will finally transfer its energy to the target plates. Computing the temperature distribution in this region is one of challenges to be faced by theory. In a stellarator the starting point is the three-dimensional heat conduction equation, however, it will be shown in the following, how this equation in Helias geometry can be reduced to a two-dimensional one. The following figure shows the boundary region in Wendelstein 7-X.

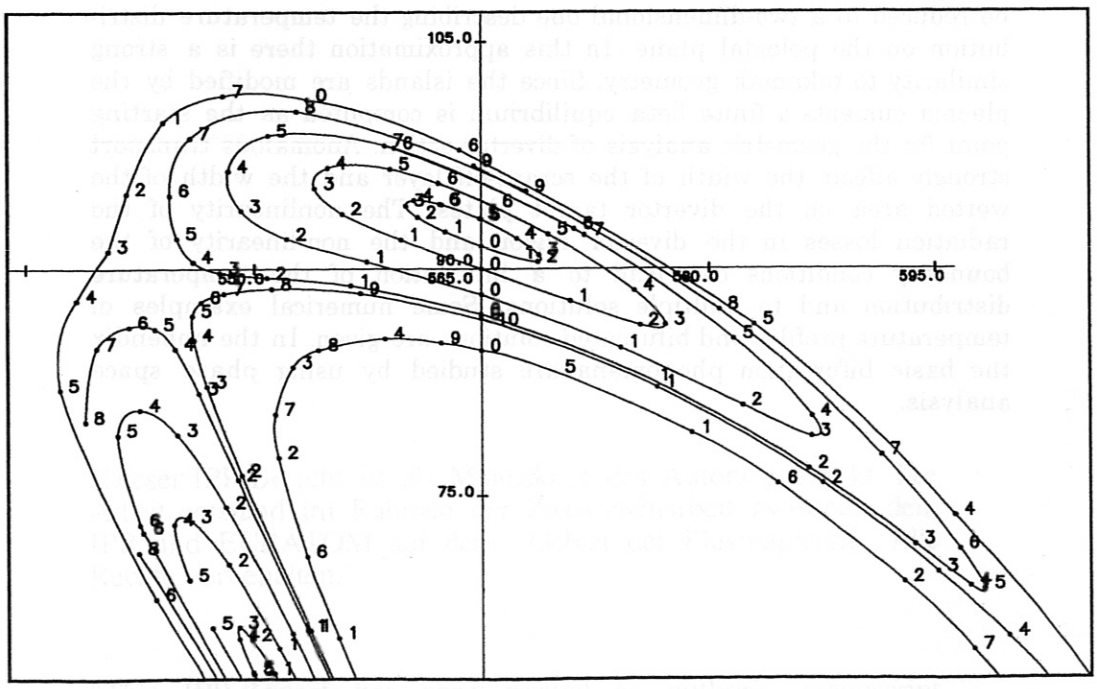

Fig. 1: Plasma boundary region in Wendelstein 7-X (vacuum field, toroidal angle φ = 0). The numbers indicate the number of toroidal transits of the field line. The starting point is 0. After three of four toroidal transits the field line arrives at the backside of the island. The islands at $\iota = 1$ are utilised for divertor action.

The magnetic islands at $\iota = 1$ helically encirculate the plasma. If described in spatial co-ordinates, the shape of these islands is not invariant, written in flux co-ordinates, however, the shape is invariant. It is expected that temperature and density distribution in the island region are almost invariant in helical direction, if target plates intersect the islands at a fixed position in flux co-ordinates. Toroidal gaps between target plates may introduce a perturbation, which must be analysed separately.

The concept of the island divertor makes use of the magnetic field structure in the island region. The plasma crossing the separatrix diffuses into the island region and after streaming parallel to the magnetic field lines it finally hits the target plates, which are located at the backside if the islands. The width of the scrap-off layer is determined by a balance between cross-field diffusion and parallel flow towards the target plates. In contrast to tokamaks the problem is three-dimensional, however in the following an attempt will be made to reduce the three-dimensional thermal conduction equation to a two-dimensional one. Furthermore, a one-dimensional approximation will be discussed, which allows one to compute the temperature profile along field lines, which are bounded by target plates. This is a model similar the two-point model of tokamaks. Due to the axisymmetry of the configuration the thermal conduction equation in tokamaks reduces to a two-dimensional equation, while in stellarator configurations approximations are needed.

2. Magnetic Islands

As seen in Fig. 1, the boundary region in Wendelstein 7-X is characterised by a set of magnetic islands around the $\iota = 1$ surface. There are five independent islands, which close upon itself after one toroidal turn. The structure of these islands in the vacuum field is shown in Fig. 1. The figure is symmetric with respect to the mid-plane, going around the torus the islands helically encircle the plasma column. In case of finite beta the plasma currents modify these islands which can be computed with the VEMEC code [8]. The following figure 2 shows the island region at $\langle\beta\rangle = 4\%$. The region around the island is highly stochastic and regular magnetic surfaces do not exist, except for a neighbourhood of the O-point of the island. In particular the region of the separatrix is highly stochastic. This feature, however, is irrelevant with respect to the plasma transport perpendicular and parallel to the field lines, since after a few number of toroidal turns the field lines intersect the target plates, while the stochasticity becomes apparent only in the limit of a large number of turns.

Magnetic islands have an internal rotational transform, which is correlated to the size of the island. The internal rotational transform grows with the size of the islands, which can be seen by a comparison of Fig. 1 and Fig. 2. Furthermore, there is a shift of the islands due to the plasma currents, the position of the target plates must be aligned to the shape of the islands in the finite beta equilibrium and not to the islands in the vacuum field.

In the following analysis we consider the magnetic field as given, although the currents in the scrap-off will contribute in shaping the magnetic field. In particular, if parallel currents between target plates exist, The may play a large role in modifying the magnetic field.

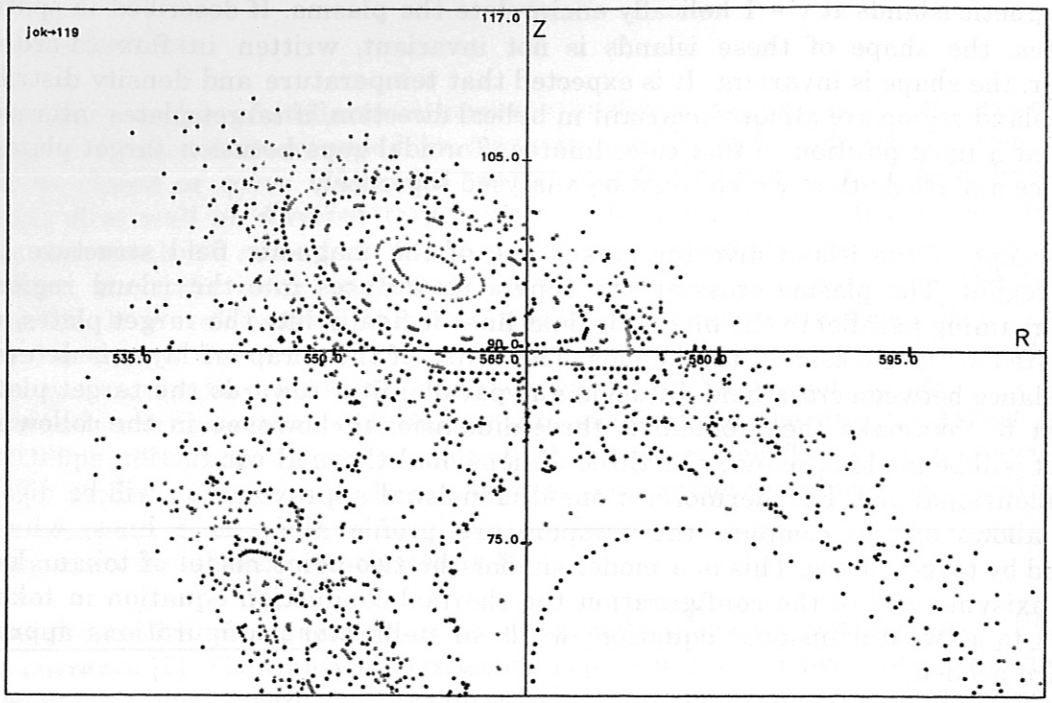

Fig. 2: Poincaré plot of magnetic islands in Wendelstein 7-X at <β> =4%.

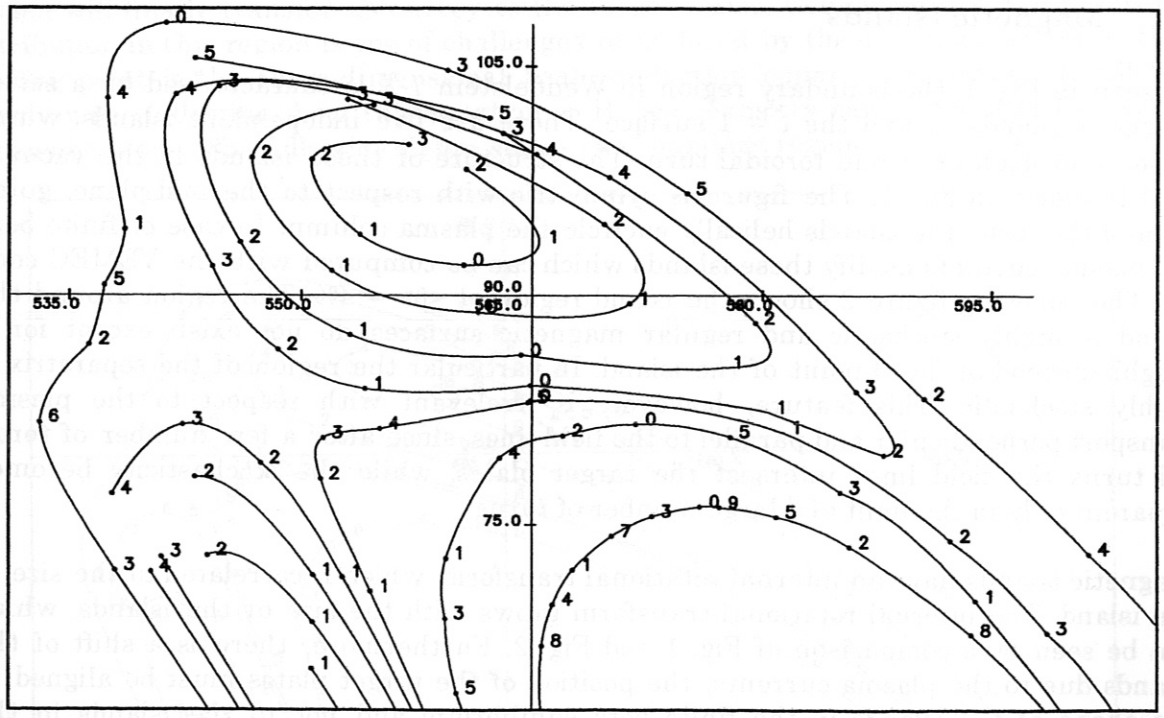

Fig. 3: Island region in Wendelstein 7-X (without divertor target plates).

In figure 3 the indices denote the number of toroidal turns; to make the laminar structure of the magnetic field more clear succeeding intersection points are connected. The internal rotaional transform of the islands grows with rising plasma pressure, which can be noticed by the reduced number of toroidal transits to reach the back side of the islands (for comparison see Fig. 1). This implies that the connection length between plasma surface and divertor target plate is decreasing with rising plasma pressure.

3. Basic Equations

In general the plasma in the scrape-off layer can only adequately be described in a multi-fluid model taking into account perpendicular and parallel transport of particles and energy. In addition, neutral particle interaction contributes to momentum and energy loss. However, to get and overview on the specific problems of three-dimensional geometry we restrict our investigation to the 3-D thermal conduction equation. Summarising the energy equations of electrons and ions and neglecting the convective terms this equation is

$$3n\frac{\partial T}{\partial t} - \nabla \bullet \chi(\boldsymbol{x},T) \bullet \nabla T = H(\boldsymbol{x},T) - Q(\boldsymbol{x},T) \qquad \text{Eq. 3.1}$$

where $H(\boldsymbol{x},T)$ is the heating term and $Q(\boldsymbol{x},T)$ the radiation loss of the electrons. The thermal conductivity is a tensor with a very large parallel conductivity.

$$\chi(\boldsymbol{x},T) = \chi_{\perp}\boldsymbol{I} + (\chi_{\parallel} - \chi_{\perp})\boldsymbol{b}:\boldsymbol{b} \qquad \text{Eq. 3.2}$$

The radiation losses are described by

$$Q(\boldsymbol{x},T) = nn_z L(T) \qquad \text{Eq. 3.3}$$

n is the electron density and n_z the density of the impurity ion. $\boldsymbol{b}$ is the unit vector along field lines. $L(T)$ is a bounded function of temperature which depends on the ion species. Since $L(T)$ is positive, continuous and bounded, it has at least one maximum at a temperature T_{max}. The density of impurities is a function of the spatial co-ordinate $\boldsymbol{x}$. Its special shape depends on the impurity species and the diffusion process of impurities. In the present context we consider the density of the impurities as a given function.

In order to facilitate the following analysis we introduce dimensionless variables. Let a be a characteristic length scale of the system, then all spatial co-ordinates are defined in units of a ($\boldsymbol{x}$ -> $\boldsymbol{x}/a$). Furthermore, let T_0 be a reference temperature and χ_0 a reference value of the thermal conductivity, then the temperature is measured in units of T_0 (T -> T/T_0). Such a reference temperature is defined by T_{max}, which is the temperature where the radiation function $L(T)$ has a maximum. Let N be a characteristic plasma density and N_Z a number to characterise the density of impurities, then the dimensionless functions are n -> n/N and n_z -> n_z/N_Z. With L_o as characteristic value of the radiation the dimensionless radiation function is $L(T)$ -> $L(T)/L_o$. In dimensionless units we write the heating function as H -> $h = Ha^2/T_o\chi_o$. In these dimensionless units the heat conduction equation is

$$n\frac{\partial T}{\partial \tau} - \nabla \bullet \chi(\boldsymbol{x},T) \bullet \nabla T = h(\boldsymbol{x},T) - \lambda p(\boldsymbol{x},T) \qquad \text{Eq. 3.4}$$

where λ is defined by

$$\lambda = \frac{a^2}{\chi_0 T_0} NN_z L_0 \quad ; \quad \tau = t\frac{\chi_0}{3a^2 N} \qquad \text{Eq. 3.5}$$

and $p(\boldsymbol{x},T)$ by

$$Q(\boldsymbol{x},T) \Rightarrow n(\boldsymbol{x})n_z(\boldsymbol{x})L(T) =: \lambda p(\boldsymbol{x},T) \qquad \text{Eq. 3.6}$$

The parameter λ is introduced as a variable or control parameter and the aim of the analysis is to study how the solution $T(\boldsymbol{x},\lambda)$ depends on this control parameter. Either the electron density N or the density N_z of impurities can be interpreted as the control

parameter λ. The control parameter grows with the size of the system. Very often the plasma pressure is considered as the independent parameter. If $nT \sim \lambda$, the function $L(T)$ is replaced by $L(T)/T$, where L(T) is of the order unity. The parallel thermal conductivity is proportional to the 5/2th power of the temperature

$$\chi_{\parallel} = \chi_0 T^{5/2} \qquad \text{Eq. 3.7}$$

which suggests to introduce a new dependent variable

$$U = \frac{2}{7} T^{7/2} \ldots; \ldots . T(U) = \left[\frac{7}{2} U\right]^{2/7} \qquad \text{Eq. 3.8}$$

The stationary equation written in these variables is

$$-\nabla \bullet \chi_{\perp}^{*}\left(x, T(U)\right) \bullet \nabla_{\perp} U - \nabla \bullet \boldsymbol{b}:\boldsymbol{b}\chi_0 \bullet \nabla U = h\left(x, T(U)\right) - \lambda p\left(x, T(U)\right) \qquad \text{Eq. 3.9}$$

with $\boldsymbol{b} = \boldsymbol{B}/B$ and

$$\chi_{\perp}^{*} = \chi_{\perp}\left(x, T(U)\right) T_U \qquad \text{Eq. 3.10}$$

In the boundary region volumetric heating is absent and only radiative losses occur on the right hand side of the equation.

$$-\nabla \bullet \chi_{\perp}^{*}\left(x, T(U)\right) \bullet \nabla_{\perp} U - \nabla \bullet \boldsymbol{b}:\boldsymbol{b}\chi_0 \bullet \nabla U = -\lambda p\left(x, T(U)\right) \qquad \text{Eq. 3.11}$$

This equation is applicable in a region of closed magnetic surface and also in regions outside the last magnetic surface where field lines terminate on target plates or the first wall. The characteristic feature of this equation is the large parallel thermal conduction, which is many orders of magnitude larger than the perpendicular thermal conduction. In this first approximation we have neglected all convective terms of the heat flux, the effect of these terms will be investigated in a later section

4. The Co-ordinate System

Because of the large asymmetry between parallel thermal transport and perpendicular transport we expect almost constant temperature on field lines. This property suggests to introduce a co-ordinate system with a parallel co-ordinate and two perpendicular co-ordinates. In order to construct such a system in the island region we start from the magnetic field in the form

$$\boldsymbol{B} = \nabla\psi \times \nabla\alpha \qquad \text{Eq. 4.1}$$

ψ = const. are the magnetic surfaces and α = const describe the field lines on magnetic surfaces. Since the field lines, in general, are not closed, the function α cannot be used as a co-ordinate. For this purpose we introduce a function η with the property that on magnetic surfaces all lines η = const. are closed after one poloidal and one toroidal transit (period 1). The choice of this co-ordinate system is not unique, any function η which has the period 1 in poloidal and toroidal direction can be used as co-ordinate surface. The rotational transform of the field

$$\boldsymbol{B}_0 = \nabla\psi \times \nabla\eta \qquad \text{Eq.4.2}$$

is unity. The entire magnetic field is

$$\boldsymbol{B} = \nabla\psi \times \nabla\eta + \delta\boldsymbol{B} \quad ; \quad \delta\boldsymbol{B} = \nabla\psi \times \nabla\left(\alpha - \eta\right) \qquad \text{Eq. 4.3}$$

$\delta \boldsymbol{B}$ is an effective poloidal field, which describes the difference between the real field and the reference field $\boldsymbol{B}_0$ with closed field lines.

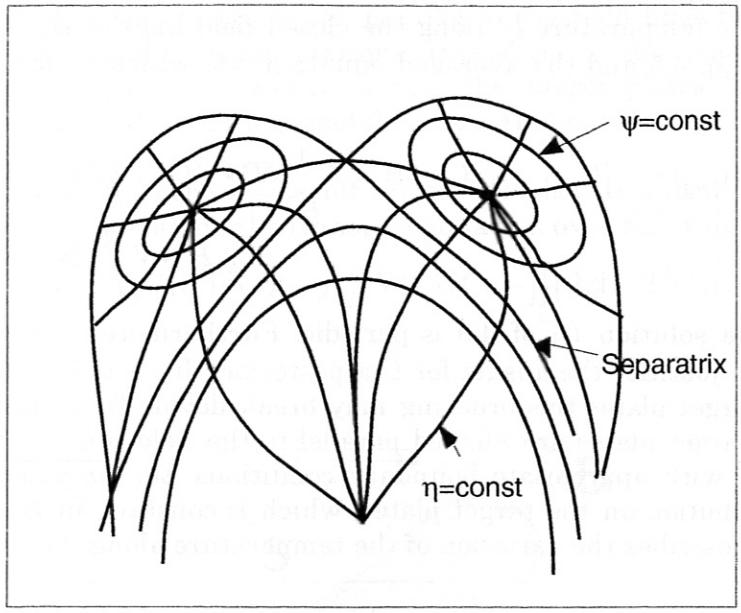

Fig. 4: Structure of the ψ,η-co-ordinate system

The small correction field is the origin of the rotational transform inside the islands. The temperature in the island region is written as

$$U = U_0(\psi,\eta) + U_1(\psi,\eta,l) \qquad \text{Eq. 4.4}$$

where l is a co-ordinate along the field lines of $\boldsymbol{B}_0$. The equation for U is

$$-\nabla \bullet \chi_\perp^*\left(\boldsymbol{x}, T(U)\right) \bullet \nabla_\perp(U) - \chi_0\left(\boldsymbol{B}_0 + \delta\boldsymbol{B}\right) \bullet \nabla \frac{1}{B^2}\left(\boldsymbol{B}_0 + \delta\boldsymbol{B}\right) \bullet \nabla U = -\lambda p\left(\boldsymbol{x}, T(U)\right) \qquad \text{Eq. 4.5}$$

Averaging this equation over the closed field lines of $\boldsymbol{B}_0$ yields

$$-<\nabla \bullet \chi_\perp^*\left(\boldsymbol{x}, T(U)\right) \bullet \nabla_\perp(U)> - \chi_0 < \delta\boldsymbol{B} \bullet \nabla \frac{1}{B^2} \boldsymbol{B} \bullet \nabla U >= -\lambda < p\left(\boldsymbol{x}, T(U)\right) > \qquad \text{Eq. 4.6}$$

The averaging procedure is defined by

$$< g >= \oint g \frac{dl}{B_0} \qquad \text{Eq. 4.7}$$

Neglecting U_1 against U_0 and the quadratic term in $\delta\boldsymbol{B}$ in combination with U_1 yields the equation for U_0

$$-<\nabla \bullet \chi_\perp^*\left(\boldsymbol{x}, T(U_0)\right) \bullet \nabla_\perp(U_0)> - \chi_0 < \delta\boldsymbol{B} \bullet \nabla \frac{1}{B^2} \delta\boldsymbol{B} \bullet \nabla U_0 >= -\lambda < p\left(\boldsymbol{x}, T(U_0)\right) > \qquad \text{Eq. 4.8}$$

This two-dimensional equation is equivalent to the heat conduction equation of tokamaks in the region outside the separatrix; in tokamaks $\delta\boldsymbol{B}$ is the poloidal field and η is the poloidal co-ordinate.

The width of the scrape-off layer is determined by a balance of thermal transport along the poloidal field towards the target plates and perpendicular transport by the first term in Eq. 4.8. The figures above show that the connection length from the plasma surface

to the target plates is a multiple of the toroidal length, which implies that the effective poloidal field in the transport equation is small.
The variation of the temperature U along the closed field lines of $\boldsymbol{B}_0$ can be found from the difference of Eq. 4.5 and the averaged equation 4.8, which in lowest order of $1/\chi_0$ yields

$$-\nabla \bullet \chi_{\perp}^{*}\left(\boldsymbol{x}, T\left(U_0\right)\right) \bullet \nabla_{\perp}\left(U_0\right) - \chi_0\left(\boldsymbol{B}_0 + \delta\boldsymbol{B}\right) \bullet \nabla \frac{1}{B^2} \delta\boldsymbol{B} \bullet \nabla U_0 + \lambda p\left(\boldsymbol{x}, T\left(U_0\right)\right) = \chi_0 \boldsymbol{B}_0 \bullet \nabla \frac{1}{B^2} \boldsymbol{B}_0 \bullet \nabla U_1 \qquad \text{Eq. 4.9}$$

Because of 4.8 the solution U_1 of 4.9 is periodic. Furthermore, the solution is of the order $o(1/\chi_0)$ which justifies the ansatz for U a posteriori. It should be noticed, however, that close to the target plates this ordering may break down. To avoid this situation we assume that the target plates are aligned parallel to the field lines of the lowest order field $\boldsymbol{B}_0$. Together with appropriate boundary conditions Eq. 4.8 yields a lowest order temperature distribution on the target plates, which is constant in $\boldsymbol{B}_0$ – direction. In a next step, eq, 4.9 describes the variation of the temperature along the target plates.

5. The Model of Flux Bundles

In the 2-D equation 4.8 two competing effects shape the temperature distribution in the island region: the first term on the right side describes an isotropic heat conduction in radial ψ-direction, while the second term describes a heat conduction in the η-direction towards the target plates. This term is proportional to χ_0 and in spite of the factor $\delta\boldsymbol{B}$ this term causes fast heat conduction towards the target plates. As a result of this effect the decay length of the scrape-off layer in ψ-direction is much smaller than the decay length in η-direction. This property can be utilised to establish the model of a flux bundle.

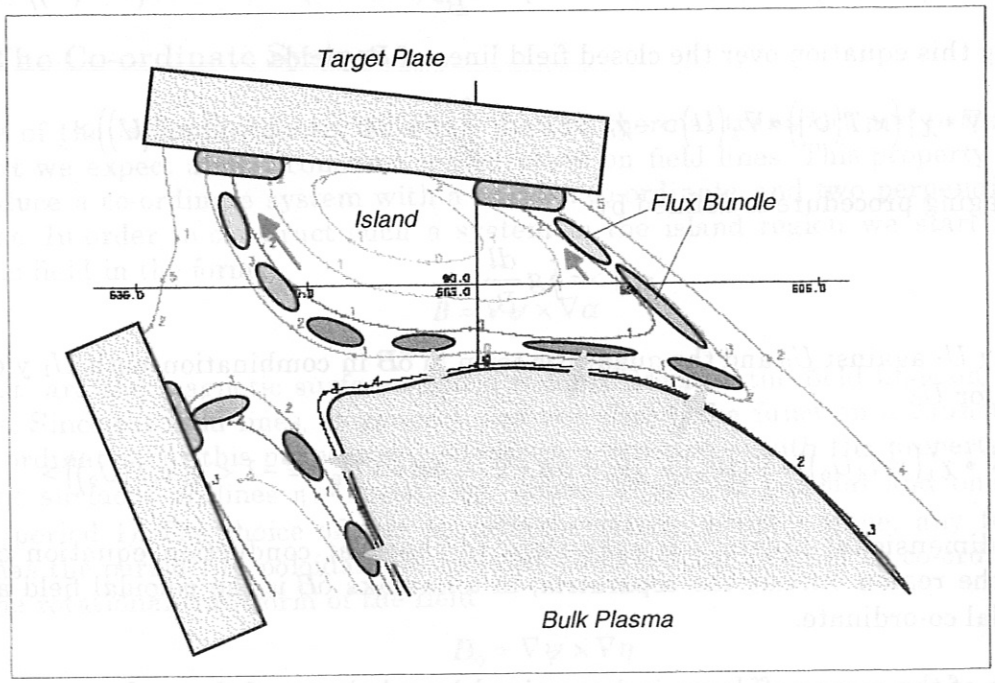

Fig. 5: Island with scrape-off layer and target plates. The flux bundles are indicated by dark ovals.
In tokamak geometry this one-dimensional model often is used to compute the temperature distribution along field lines between two target plates [9,10,11]. In the following

we will derive an equivalent equation for the field lines in the islands of a stellarator. For this purpose we consider field lines in the islands which are displayed in figure 5.1. The heat flux across the separatrix moves parallel to the field lines towards the target plates. Because of the small internal rotational transform of the islands the field lines need five or more toroidal turns before hitting the target plates. The width of the scrape-off is small compared with the poloidal and parallel decay length.

Let us consider a flux tube in the scrape-off region, which is bounded by two surfaces F as indicated in Fig. 5.2. Averaging the transport equation over this volume yields

$$-\iint_S \nabla_\perp U \bullet \chi_\perp^*\left(\boldsymbol{x}, T(U)\right) \bullet d\boldsymbol{f} - \chi_0 \iint_F \nabla U \bullet d\boldsymbol{f} = -\iiint_V \lambda p\left(\boldsymbol{x}, T(U)\right) d^3\boldsymbol{x} \qquad \text{Eq. 5.1}$$

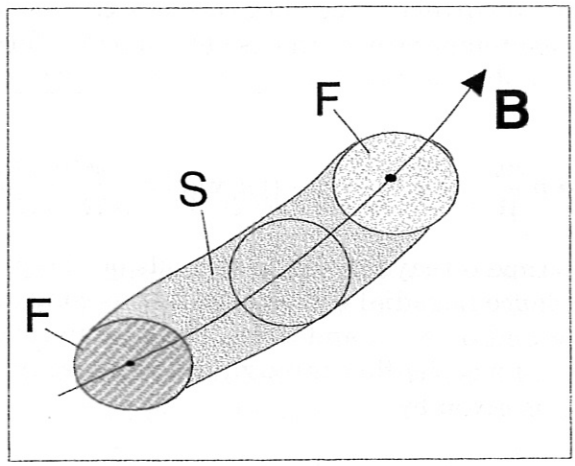

Fig. 6: Flux tube in the island region. The magnetic field is tangential to the surfaces S and perpendicular to the surfaces F. The limits in flux coordinates are $\psi,\psi+\delta\psi$ and $\alpha,\alpha+\delta\alpha$.

The first term is the heat flux through the boundary surface S and the second one is the parallel heat flux through F. This term is the difference of the two integrals over S. The magnetic field in the island region is close to a vacuum field and we may introduce the magnetic potential Φ as a co-ordinate along field lines. The surfaces F are defined by Φ = const. ($\Phi = \Phi_1$ and $\Phi = \Phi_2$). The volume element is given by

$$d^3\boldsymbol{x} = df \frac{d\Phi}{B} = \frac{d\psi d\alpha d\Phi}{B^2} \qquad \text{Eq. 5.2}$$

and the parallel gradient is

$$\boldsymbol{B} \bullet \nabla = B^2 \frac{\partial}{\partial \Phi} \qquad \text{Eq. 5.3}$$

Note that α is the poloidal flux function of the total magnetic field as defined in Eq. 4.1. The cross section of a flux tube is defined by $\psi,\psi+\delta\psi$ and $\alpha,\alpha+\delta\alpha$. Using these co-ordinates leads to

$$\nabla \bullet \boldsymbol{b}:\boldsymbol{b}\chi_0 \bullet \nabla U = \chi_0 B^2 \frac{\partial^2 U}{\partial \Phi^2} \qquad \text{Eq. 5.4}$$

Integrating over the volume of the flux tube yields

$$\iiint_V \nabla \bullet \boldsymbol{b}:\boldsymbol{b}\chi_0 \bullet \nabla U d^3x = \chi_0 \iiint \frac{\partial^2 U}{\partial \Phi^2} d\psi d\alpha d\Phi \qquad \text{Eq. 5.5}$$

In the limit Φ_2-$\Phi_1 = \delta\Phi$ -> 0 the flux tube equation 5.1 becomes

$$-\oint_F \nabla_\perp U \bullet \chi_\perp^* \bullet \boldsymbol{n} \frac{ds}{B} - \chi_0 F_0 \frac{\partial^2 \overline{U}}{\partial \Phi^2} = -\iint_F \lambda p\left(\boldsymbol{x}, T\left(U\right)\right) \frac{d\psi d\alpha}{B^2} \qquad \text{Eq. 5.6}$$

$\boldsymbol{n}$ is the normal vector on the flux tube. The line integral in the first term extends over the boundary of F, it describes the heat flux into the flux tube with the length $\delta\Phi$. The average of U is defined by

$$\overline{U} = \frac{1}{F_0} \iint_F U d\psi d\alpha ...; ... F_0 = \iint_F d\psi d\alpha \qquad \text{Eq. 5.7}$$

This equation describes the variation of the average temperature in the flux tube, however, the task remains to correlate the flux through the surface S and the average radiation loss to the average temperature. In case of a narrow flux tube we may replace the temperature U in the radiation function by its average value and the equation 4.6 reads

$$-\oint_F \nabla_\perp U \bullet \chi_\perp^* \bullet \boldsymbol{n} \frac{ds}{B} - \chi_0 F_0 \frac{\partial^2 \overline{U}}{\partial \Phi^2} = -\iint_F n\left(\boldsymbol{x}\right) n_z\left(\boldsymbol{x}\right) \frac{d\psi d\alpha}{B^2} L\left(T\left(\overline{U}\right)\right) \qquad \text{Eq. 5.8}$$

The temperature in the scrape-off layer weakly depends on the perpendicular variable α and it has a strong dependence in radial ψ-direction. Let us consider a flux tube, which is bounded by the surfaces ψ and $\psi + \delta\psi$, α and $\alpha + \delta\alpha$. The dominating term in the heat flux on the left hand side of Eq. 4.8 is the flux through the surfaces ψ = const. The heat flux into the surface ψ = const. is given by

$$q\delta\alpha = -\int_{\psi=const} \nabla_\perp U \bullet \chi_\perp^* \bullet \boldsymbol{n} \frac{ds}{B} \qquad \text{Eq. 5.9}$$

and Eq. 4.8 can be written as

$$\left(q\left(\psi + \delta\psi\right) - q\left(\psi\right)\right)\delta\alpha - \chi_0 F_0 \frac{\partial^2 \overline{U}}{\partial \Phi^2} = -\iint_F n\left(\boldsymbol{x}\right) n_z\left(\boldsymbol{x}\right) \frac{d\psi d\alpha}{B^2} L\left(T\left(\overline{U}\right)\right) \qquad \text{Eq. 5.10}$$

The problem is to correlate the radial heat flux to the average temperature in the flux tube. Let us consider a flux tube in the scrape-off layer, which is bounded by the separatrix and the outer boundary of the SOL. The poloidal width of this flux tube is determined by the internal rotational transform of the islands. This flux tube (denoted by 0 in Fig. 4.1) maps onto 1 after one toroidal turn and onto 2 after the next turn and so on. After several toroidal turns the flux tube intersects the target plate. Since the lower boundary of the flux tube is close to separatrix the input flux is known: $q(\psi) = q_{in}(\psi)$. The upper boundary is defined by q = 0, since the whole input flux has left the scrape-off layer by parallel heat conduction or by radiation. In this approximation the parallel transport equation is

$$-\chi_0 F_0 \frac{\partial^2 \overline{U}}{\partial \Phi^2} = q_{in}\left(\Phi\right)\delta\alpha - \iint_F n\left(\boldsymbol{x}\right) n_z\left(\boldsymbol{x}\right) \frac{d\psi d\alpha}{B^2} L\left(T\left(\overline{U}\right)\right) \qquad \text{Eq. 5.11}$$

The geometry of this flux tube is sketched in the following figure.

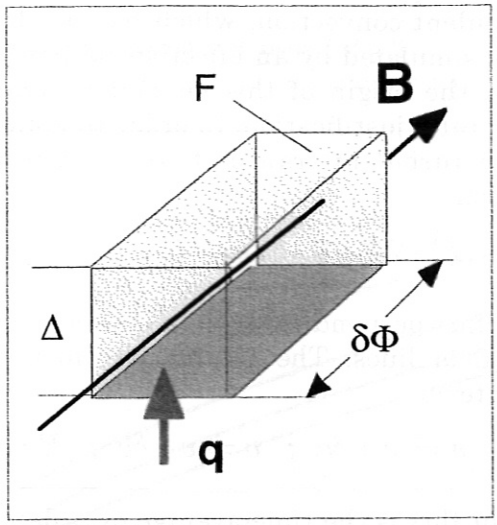

Fig. 7: Flux tube in the scrape off layer. Plasma inflow **q** occurs from the lower side.

These approximations have reduced the heat conduction equation to a one-dimensional equation in standard form. The variation of the magnetic field along the flux tube has eliminated by introducing the magnetic potential as independent variable. The approximation in Eq. 4.11 can be slightly improved by assuming a linear ψ-dependence of $q(\psi)$. Let Δ be the width of the SOL in ψ-coordinates, then we get

$$\left(q\left(\psi+\delta\psi\right)-q\left(\psi\right)\right)\delta\alpha \approx \frac{q_{in}}{\Delta}\delta\psi\delta\alpha \qquad \text{Eq. 5.12}$$

and the transport equation becomes

$$-\chi_0 \frac{\partial^2 \overline{U}}{\partial \Phi^2} = \frac{1}{\Delta} q_{in}\left(\Phi\right) - \frac{1}{F_0}\iint_F n\left(\boldsymbol{x}\right) n_z\left(\boldsymbol{x}\right) \frac{d\psi d\alpha}{B^2} L\left(T\left(\overline{U}\right)\right) \qquad \text{Eq. 5.13}$$

This approximation implies that the power deposited in all flux tube is the same.

The solution of this equation 5.13 requires boundary conditions, which are defined by the physics processes in front of the target plates. In general these boundary conditions are a non-linear relation between the temperature and the temperature gradient on the boundary.

$$g\left(U, \nabla U\right) = 0 \qquad \text{Eq. 5.14}$$

Special cases of such boundary conditions are

$$\chi_0 \frac{\partial \overline{U}}{\partial \Phi}\Big|_0 = \alpha \overline{U}^s\left(0\right) \quad ; \quad \chi_0 \frac{\partial \overline{U}}{\partial \Phi}\Big|_1 = \beta \overline{U}^s\left(1\right) \qquad \text{Eq. 5.15}$$

s is a constant, which in case of constant pressure along the flux tube is $s = 1/7$. α,β are constants, which are determined by the transition process at the divertor target plates.

6. Anomalous Transport

In the preceeding section convective losses have been neglected. However, it is a well known from divertor experiments that the width of the scarpe-off layer is dominated by

anomalous perpendicular transport rather than by classical thermal conduction. The reason is stationary or turbulent convection, which has not been retained above. Often this anomalous transport is simulated by an effective perpendicular thermal conduction in numerical studies, since the origin of this anomalous transport is convection, this approximation requires a careful justification. In order to obtain a rough estimate about the influence of convective turbulent transport we start from the transport equation including the convective term.

$$-\nabla \bullet \chi\left(\boldsymbol{x}, T\right) \bullet \nabla T + \nabla \bullet 5Tn\boldsymbol{v} = h\left(\boldsymbol{x}, T\right) - \lambda p\left(\boldsymbol{x}, T\right) \qquad \text{Eq. 6.1}$$

$n\boldsymbol{v}$ is the turbulent particle flux perpendicular to magnetic field lines and the convective transport along magnetic field lines. The plasma parameters are written as a time-averaged and a fluctuating term

$$\boldsymbol{b} \Rightarrow \boldsymbol{b}_0 + \delta\boldsymbol{b} \;\; ; \;\; n \Rightarrow n + \delta n \;\; ; \;\; \boldsymbol{v} \Rightarrow \boldsymbol{v} + \delta\boldsymbol{v} \;\; ; \;\; \boldsymbol{E} \Rightarrow \delta\boldsymbol{E} \qquad \text{Eq. 6.2}$$

The perpendicular turbulent flux is the time-average over density fluctuations times the fluctuations of the velocity $\boldsymbol{v}$.

$$n\boldsymbol{v}_\perp = \; < \delta n \delta \boldsymbol{v} > \; = \frac{\boldsymbol{1}}{B^2} < \delta n \delta \boldsymbol{E} \times \boldsymbol{B} > \qquad \text{Eq. 6.3}$$

Here we assumed that the electric drift of the plasma particles causes the turbulent flux. The convective term along magnetic field lines is $Tn\boldsymbol{v}_{\|}$, which must be computed from the momentum balance along field lines [12]. Magnetic fluctuations may also contribute to anomalous transport, in particular, at the beta limit MHD-instabilities are to be expected giving rise to $\delta\boldsymbol{B}$ - fluctuations. The perpendicular component of these magnetic fluctuations has the same effect as the steady state poloidal field. Together with the large parallel thermal conductivity these fluctuations may lead to a strong perpendicular thermal transport.

If there are no ionisation and recombination processes in the divertor region the equation of continuity yields

$$\nabla \bullet < n\boldsymbol{v} > \; = 0 \;\; \Rightarrow \;\; < \nabla \bullet Tn\boldsymbol{v} > \; = \; < n\boldsymbol{v} > \bullet \nabla T \qquad \text{Eq. 6.4}$$

The time average of the first term in Eq. 6.1 is

$$< \nabla \bullet \chi\left(\boldsymbol{x}, T\right) \bullet \nabla T > \; = \nabla \bullet \chi_\perp^*\left(\boldsymbol{x}, T\left(U\right)\right) \bullet \nabla_\perp U - \nabla \bullet \chi_0 < \frac{\left(\delta B\right)^2}{B^2} > \bullet \nabla U - \nabla \bullet \boldsymbol{b}_0 : \boldsymbol{b}_0 \chi_0 \bullet \nabla U$$

Where the transition from T to the variable U has been made.

Also magnetic fluctuations can be the reason for enhanced perpendicular conductivity

$$\chi_{eff} = \chi_0 < \frac{\left(\delta B\right)^2}{B^2} > \qquad \text{Eq. 6.5}$$

As an example we consider the boundary region of Wendelstein 7-X and assume a temperature in the order of 100 – 300 eV. The parallel thermal diffusivity of electrons in this region is shown in Fig. 8.
The ion thermal diffusivity is smaller than the electron diffusivity; it is in the order of 10^6 m²/s. The results show that magnetic fluctuations in the order of $\delta B/B = 10^{-4}$ can lead to an effective perpendicular thermal conductivity of the eletrons in the order of 1 m²/s. The effective ion thermal conduction is smaller by two orders of magnitude. The derivation shows that magnetic fluctuations can be described by an enhanced thermal conductivity, which is in contrast to the effect of electric perturbations.

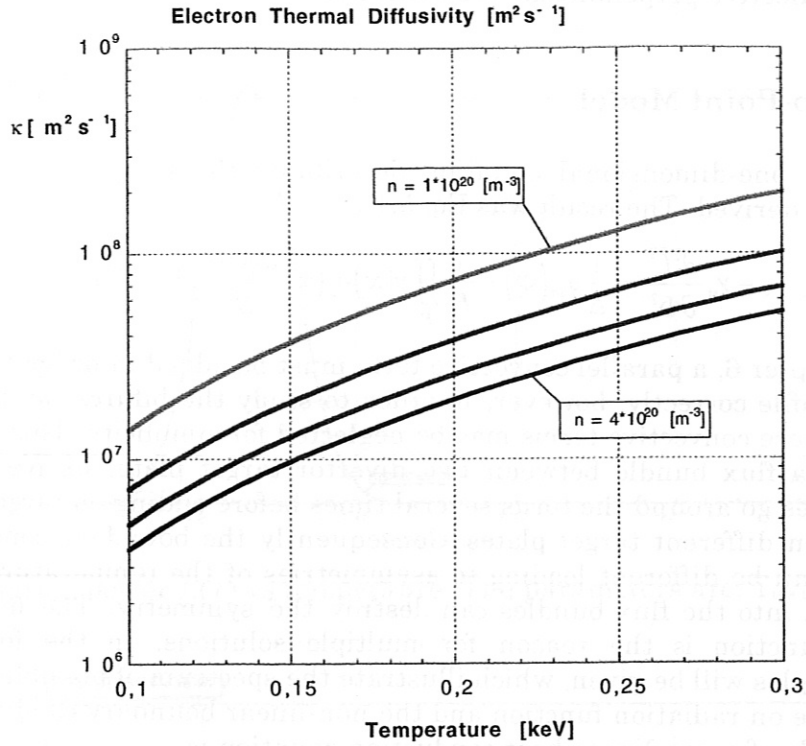

Fig. 8: Parallel thermal diffusivity κ of electrons in the temperature regime from 100 to 300 eV. The density is (1 – 4) 10^{20} m^{-3}. The thermal conductivity is χ=nκ.

In order to assess the effect of electric fluctuations we assume that temperature fluctuations are negligible. The poloidal components of the fluctuating ***E***-field contribute to radial transport and to a widening of the scrape-off layer. It should be noted that anomalous transport cannot be interpreted in terms of an anomalous thermal conductivity, because this depends on the first order derivative of the temperature, while the conductive term has second order derivatives. Transforming the temperature T -> U yields the convective term

$$5n\boldsymbol{v}\bullet\nabla T = 5n\boldsymbol{v}\bullet\frac{dT}{dU}\nabla U \qquad \text{Eq. 6.6}$$

which has to be added to the conductive term. The sum of the anomalous fluxes is then

$$-\chi_0 < \frac{(\delta B)^2}{B^2} > \bullet\nabla U + 5n\boldsymbol{v}_\perp T(U) \qquad \text{Eq. 6.7}$$

Experimental observations in the boundary region of current experiments suggest that the anomalous transport is much larger than the classical transport and the classical perpendicular transport is negligible in Eq. 6.3. The transport equation reduces to

$$-\nabla\bullet\chi_0 < \frac{(\delta B)^2}{B^2} > \bullet\nabla U - \nabla\bullet\boldsymbol{b}_0 : \boldsymbol{b}_0\chi_0\bullet\nabla U + 5n\boldsymbol{v}\bullet\nabla T(U) = h\left(\boldsymbol{x}, T(U)\right) - \lambda p\left(\boldsymbol{x}, T(U)\right) \qquad \text{Eq. 6.8}$$

Often in the literature the ansatz is made that the anomalous transport flux is proportional to the local temperature gradient or the density gradient. This would introduce another first order derivative in Eq. 6.1, but not a second order derivative. Describing the effect of electric fluctuations in terms of an effective thermal conductivity is not

justified. In contrast to electric fluctuations the influence of magnetic fluctuations can be replaced by an effective perpendicular conductivity.

7. The Two-Point Model

In chapter 5 an one-dimensional equation describung the temperature along a flux bundle has been derived. The result was Eq. 5.13

$$-\chi_0 \frac{\partial^2 \overline{U}}{\partial \Phi^2} = \frac{1}{\Delta} q_{in}(\Phi) - \frac{1}{F_0} \iint_F n(\boldsymbol{x}) n_z(\boldsymbol{x}) \frac{d\psi d\alpha}{B^2} L\left(T\left(\overline{U}\right)\right) \qquad \text{Eq. 7.1}$$

As shown in chapter 6, a parallel convective term must be added in order to describe the temperature profile correctly, however, in order to study the bifurcation phenomena of this equation, these convective terms may be neglected for simplicity. This plasma model is applicable to a flux bundle between two divertor target plates of Wendelstein 7-X. since flux bundles go around the torus several times before ending on target plates, they begin and end on different target plates. Consequently the boundary conditions on the two endpoints can be different leading to asymmetries of the temperature profile. Also the power input into the flux bundles can destroy the symmetry. The non-linearity of the radiation function is the reason for multiple solutions. In the following some numerical examples will be given, which illustrate the spectrum of possible solutions and their dependence on radiation function and the non-linear boundary conditions.
A simple example of a non-linear heat conduction equation is

$$-\chi \frac{\partial^2 T}{\partial r^2} = h(r) - \lambda p(T, r) \qquad \text{Eq. 7.2}$$

in the intervall [0,1]. The model of boundary conditions is

$$\varepsilon \left[T'(a)\right]^{xp} = T \qquad \text{Eq. 7.3}$$

ε and xp are constants. Setting ε to zero would yield the standard Dirichlet boundary conditions. Then bifurcation is only possible due to the non-linearity of the radiation function. This is modelled by the following equation.

$$p(T,r) = g(r)\left[\exp\left(-\frac{1}{w1}\left(T - T_{\max 1}\right)^2\right) + F\exp\left(-\frac{1}{w2}\left(T - T_{\max 2}\right)^2\right)\right] \qquad \text{Eq. 7.4}$$

This radiation function has two maxima (at T_{max1} and T_{max2}), the width of the two maxima is determined by $w1$ and $w2$. $g(r)$ stands for the product of electron density and impurity density. In principle a diffusion equation is needed to compute the density of impurities, here we consider the distribution of g(r) as a given function. The heating function is symmetric around r_0=0.5 and has the form

$$h(r) = h_0 \exp\left[-\left(r - r_0\right)^2 / w\right] \qquad \text{Eq. 7.5}$$

Example 1: Constant heating on flux tube

In the first example we model a radiation function with one maximum only and keep the heating power over the whole region [0<r<1] equal to a constant. The radiation function is shown in the following figure, the function g(r) is constant, too

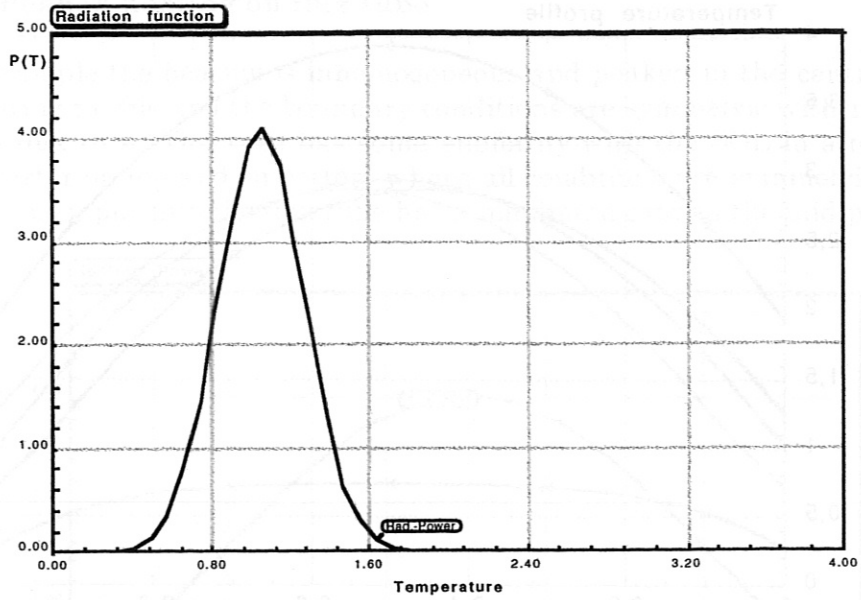

Fig. 9: Radiation power $L(T)$ vs temperaure. The parameters are: $T_{max\,1}$= 1, w1 = 0.1, g(r) = const.

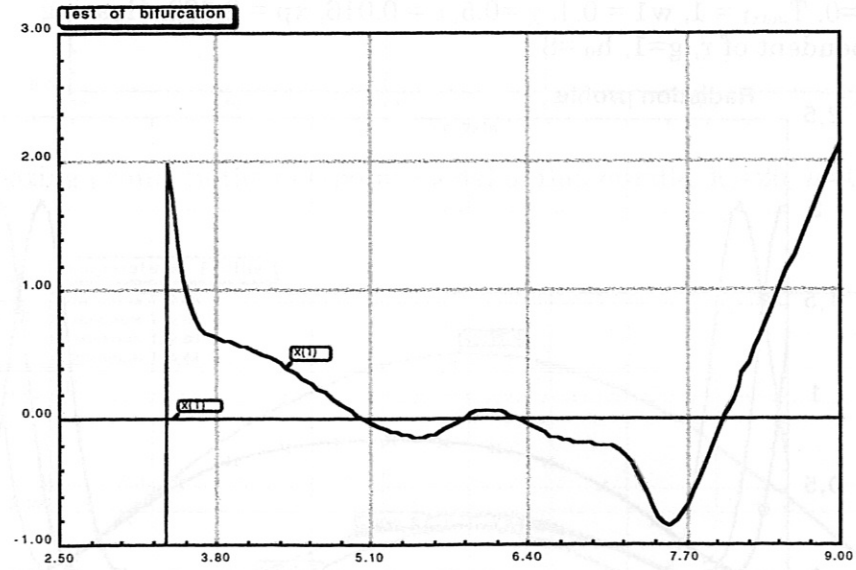

Fig. 10: Test of boundary conditions. Crossing the zero line determines a solution.

A shooting method is applied to solve the differential equation together with the boundary conditions. For this purpose the equation is converted into two first order equations, which are solved by Rung-Kutta integration. The integration starts at r = 0 with the slope of the temperature T' as a variable parameter. This slope is the x-axis in Fig. 10. The temperature at r = 0 is given by the boundary condition. Integrating the equations until the right boundary r = 1 is reached yields the temperature and its derivative on the right hand side. These data are used to test the boundary conditions on the right hand side. Every time the test function in Fig 10 is zero, the boundary conditions are satisfied. This method yields all solutions of the differential equation, the stable and the unstable ones. In this respect it is superior to methods, which solve the time-dependent heat conduction equation; these only provide the stable solutions.

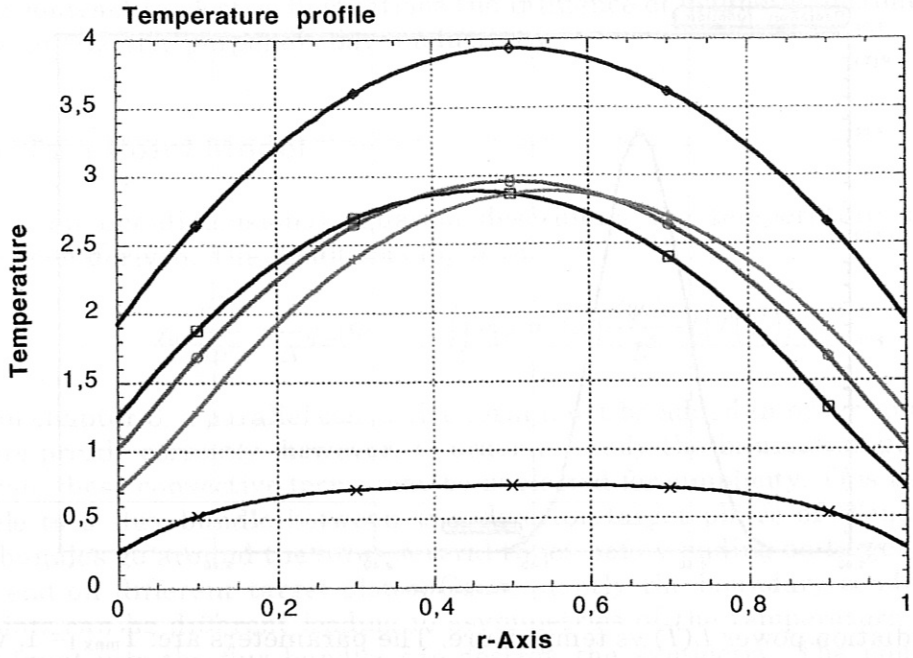

Fig. 11: Temperature profile in the flux bundle between target plates. λ = 20, F=0, T_{max1} = 1, w1 = 0.1, χ =0.5, ε = 0.016, xp = 2.333. Heating independent of r, g=1, h_0 =8

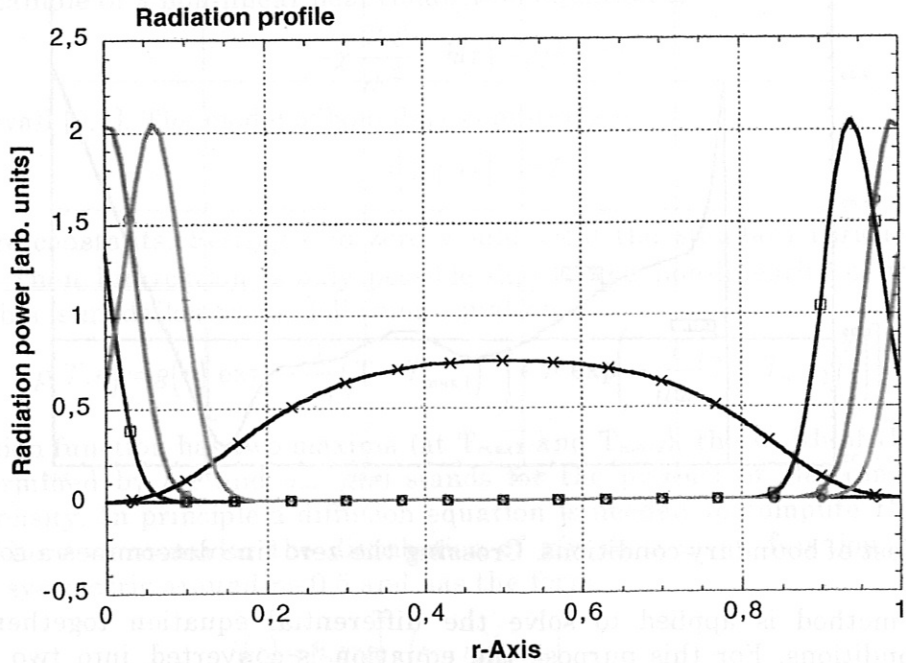

Fig. 12: Radiation profiles for case of Fig. 11.

Some of the profiles are asymmetric although the heating function is symmetric. There are 5 solutions, which are caused by the various non-linearities; an analytical study of this effect is given in the appendix. The radiation function in this example has one maximum in temperature, this would provide one or three solutions, if the temperature is fixed on the target plates (Dirichlet boundary conditions). Due to the non-linear boundary conditions two further solutions exist. Such a temperature drop between two target plates, connected by a flux tube, can give rise to plasma currents between the target plates.

Example 2: Peaked heating on flux tube

In the next example the heating is inhomogeneous and peaked in the centre of the flux tube. The heating profile and the boundary conditions are symmetric with respect to the middle of the flux tube. This case has some similarity with the SOL in a tokamak with an X-type divertor on top and on bottom where all conditions are symmetric to the mid-plane. The power input into the flux tube has a maximum around the mid-plane.

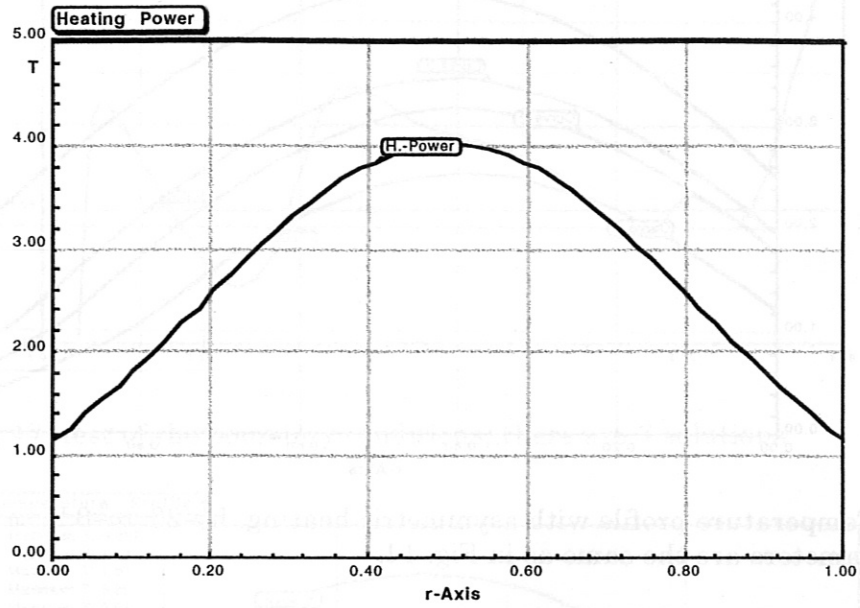

Fig. 13: Heating profile in the two-point model of flux bundle. h_0=20, w=0.2. x_0 = 0.5

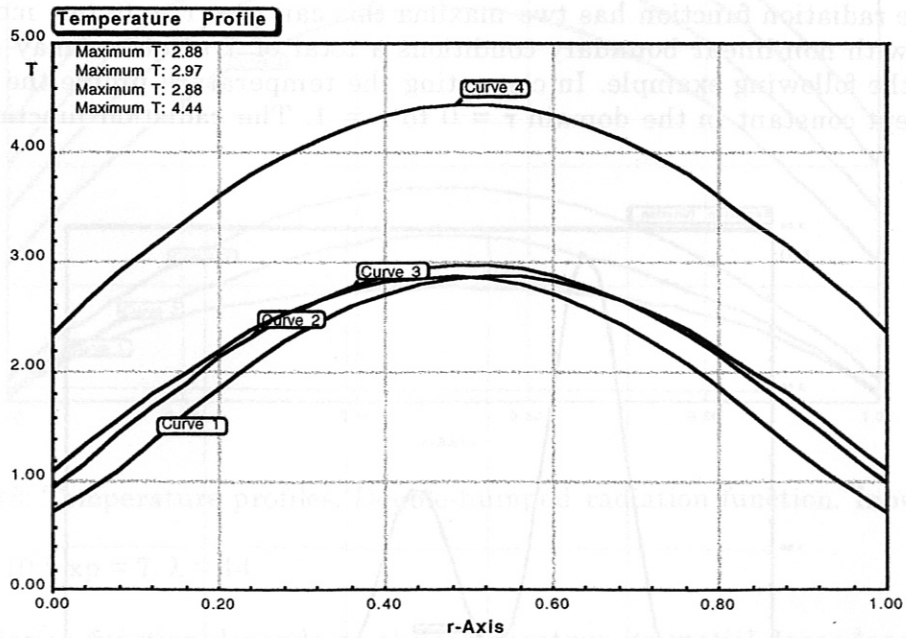

Fig. 14: Temperature profiles. Radiation function 1: $\lambda = 35$, $T_{max1} = 1$, w1 = 0.1, F = 0, χ = 1,
$\varepsilon = 0.025$, xp = 2.333. The solution with the lowest temperature is not shown.

Example 3: Asymmetric heating

If the heating profile is asymmetric this also causes the temperature profiles to show similar asymmetries.

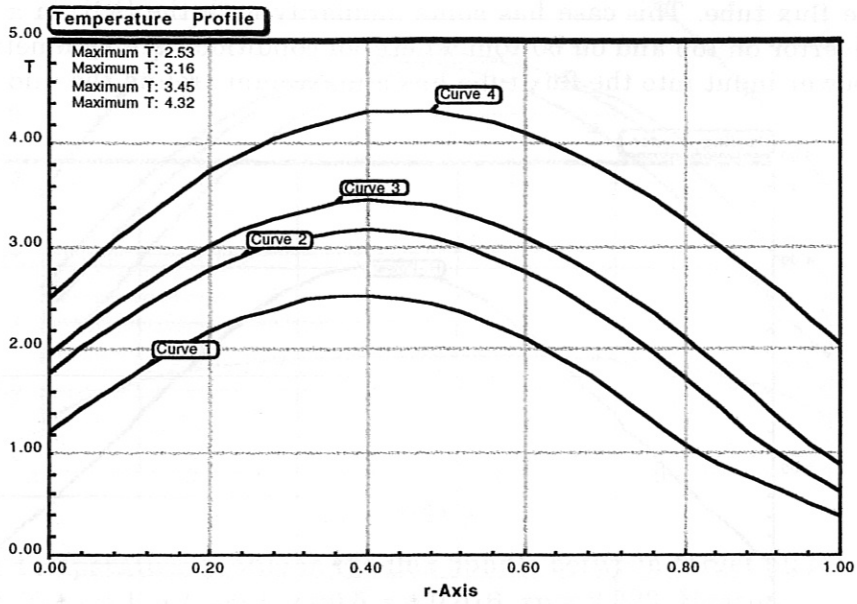

Fig. 15: Temperature profile with asymmetric heating. h_0=20, w=0.2. x_0 = 0.4. The other parameters are the same as in Fig. 14.

Example 4: Radiation function with two maxima

In case the radiation function has two maxima this can give rise to two more solutions. Together with non-linear boundary conditions a total of 7 solutions may exist. This is shown in the following example. In computing the temperature profile the power deposition is kept constant in the domain r = 0 to r = 1. The radiation function is double-humped.

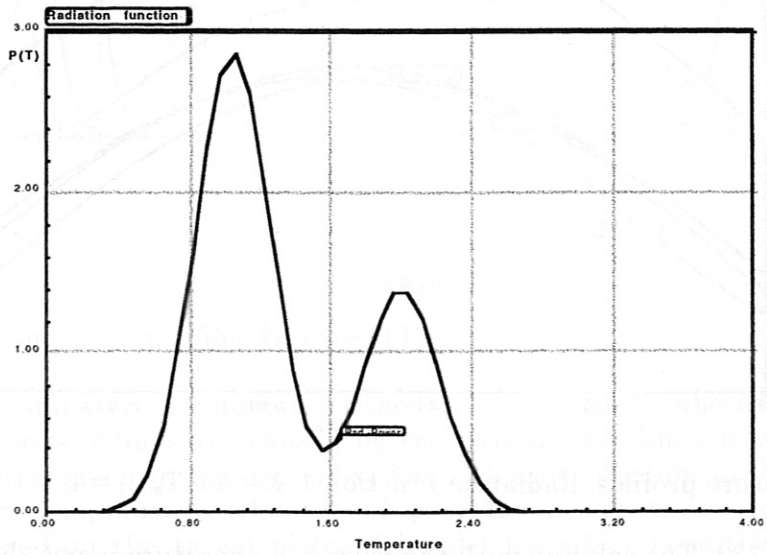

Fig. 16: Radiation function vs temperature. Parameters: T_{max1} = 1, T_{max2} = 2, λ = 14, F = 0.5, w1 = w2 = 0.1

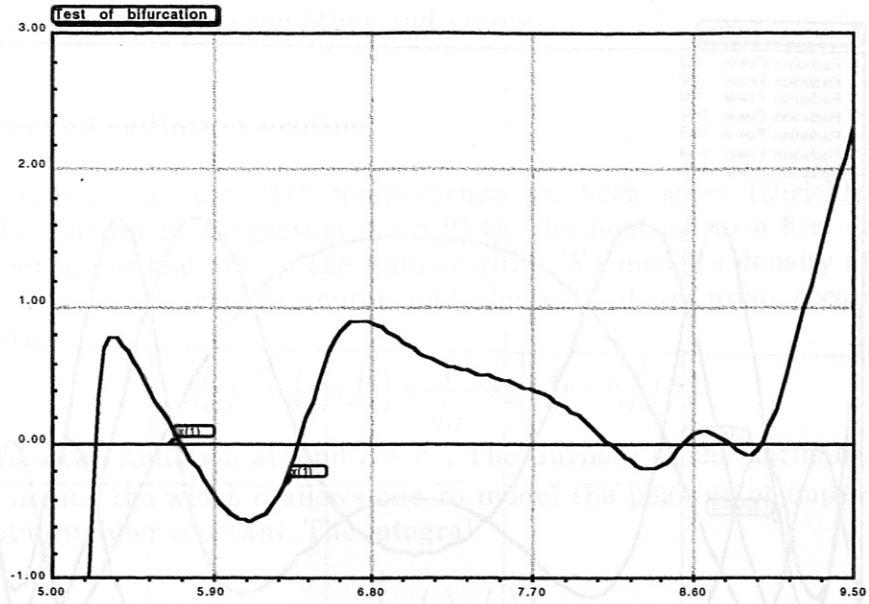

Fig. 17: test of the boundary conditions, there are 7 solutions

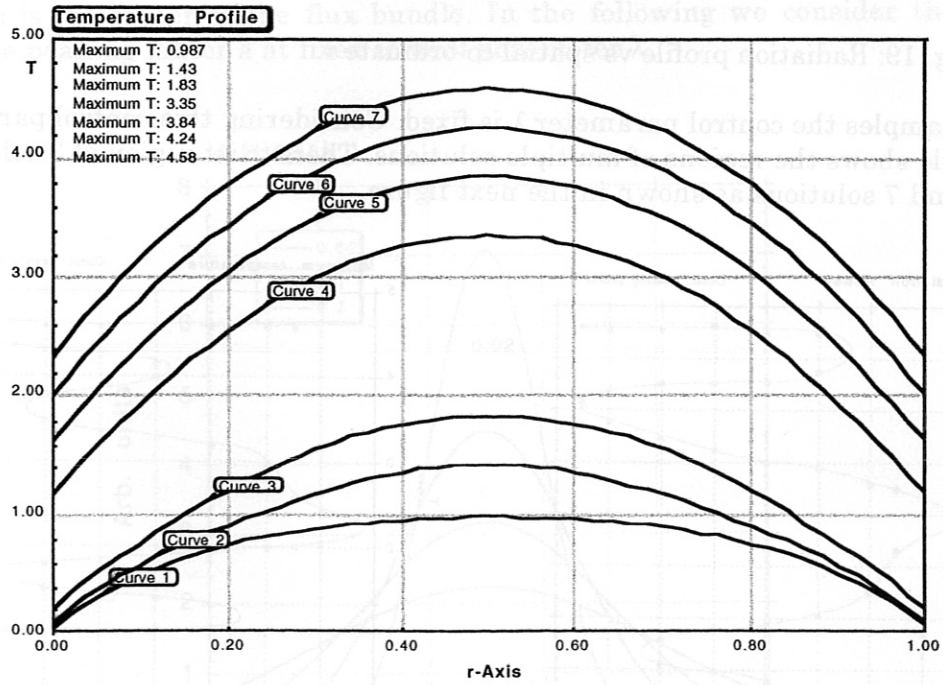

Fig. 18: Temperature profiles. Double-humped radiation function. Input data:
$\varepsilon = 5\ 10^{-7}$, xp = 7, $\lambda = 14$.

Since the radiation function depends on the temperature its spatial dependence is fixed by the temperature profile alone. At low temperature the maximum of the radiation is centered to the middle of the flux bundle. With rising temperature the maxima are shifted more towards the target plates

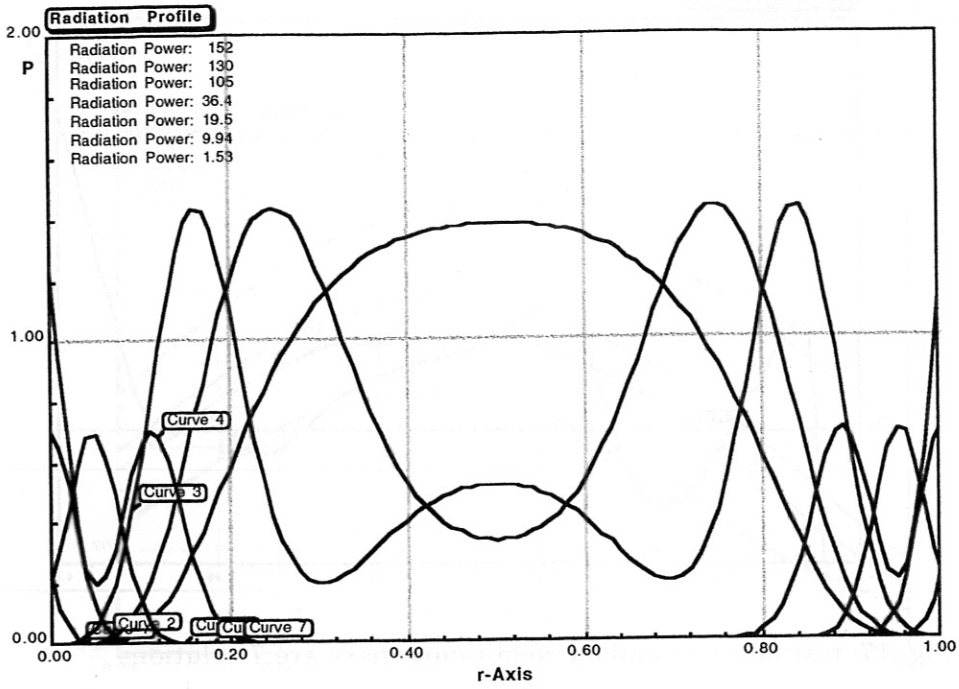

Fig. 19: Radiation profile vs spatial co-ordinate r.

In these examples the control parameter λ is fixed. Considering this control parameter as a variable shows the regions of multiple solutions. There exist region of 3 solutions, 5 solutions and 7 solutions as shown in the next figure.

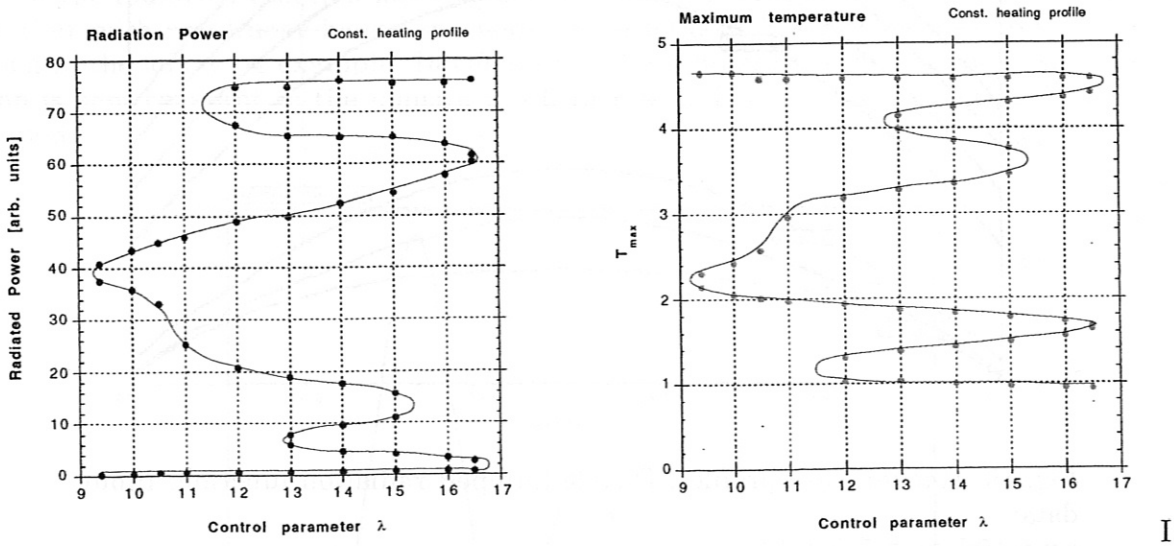

Fig. 20: Max. temperature (right 20b) and radiation power (left 20a) vs control parameter λ.

These figures show the spectrum of possible solutions vs the radiation factor λ. In a region of λ between $13 < \lambda < 15$ 7 solutions exist. Outside this domain 5 solutions or 3 solutions exist. The solution is unique if the control parameter is small enough (smaller than 9). The figure 20a shows the radiated power vs the control parameter. The branch with the highest temperature is independent of the control parameter. The temperature (20b) lies above the maximum radiation temperature T_{max2} and therefore the solutions are nearly unaffected by the radiation losses, the radiation is nearly zero (see lower

branch in Fig.20a). There are 6 bifurcation point in the λ-regimes, these are the points where two solutions approach each other and merge.

Example 5: Peaked radiation profiles

The boundary conditions are zero temperature on both sides (Dirichlet boundary conditions). The domain of integration is r = [0,1]. The heating term h(r) depends only on the space coordinate and not on the temperature. We model a density of impurities, which are peaked in the plasma center and choose a distribution according to the following equation

$$g(r) = n_e(r)n_z(r) = \frac{1}{\sqrt{a}}\exp\left[-(r-r_1)^2/a\right] \qquad \text{Eq. 7.6}$$

The model peaks the radiation around $r = r_1$. The purpose of the normalising factor is the following: variing the width a allows one to model the peaking of impurity ions and keeping the total number constant. The integral

$$\int_0^1 n_e(r)n_z(r)dr \qquad \text{Eq. 7.7}$$

is kept fixed under the variation of a. The density of impurities has a maximum at r = 0.5, which is the center of the flux bundle. In the following we consider the effect of variing the peaking faktor a at fixed control parameter λ.

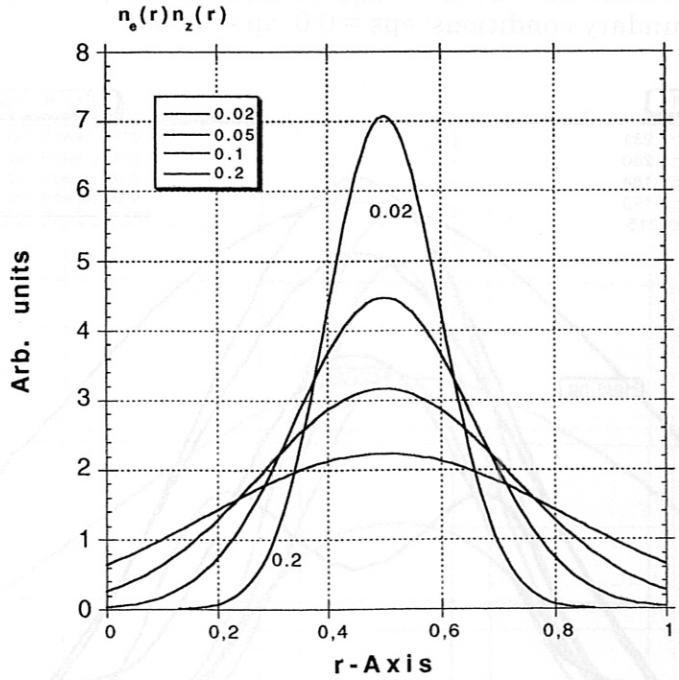

Fig. 21: Radial distribution of $n_e(r)n_z(r)$. The parameter of the curves is the width a.

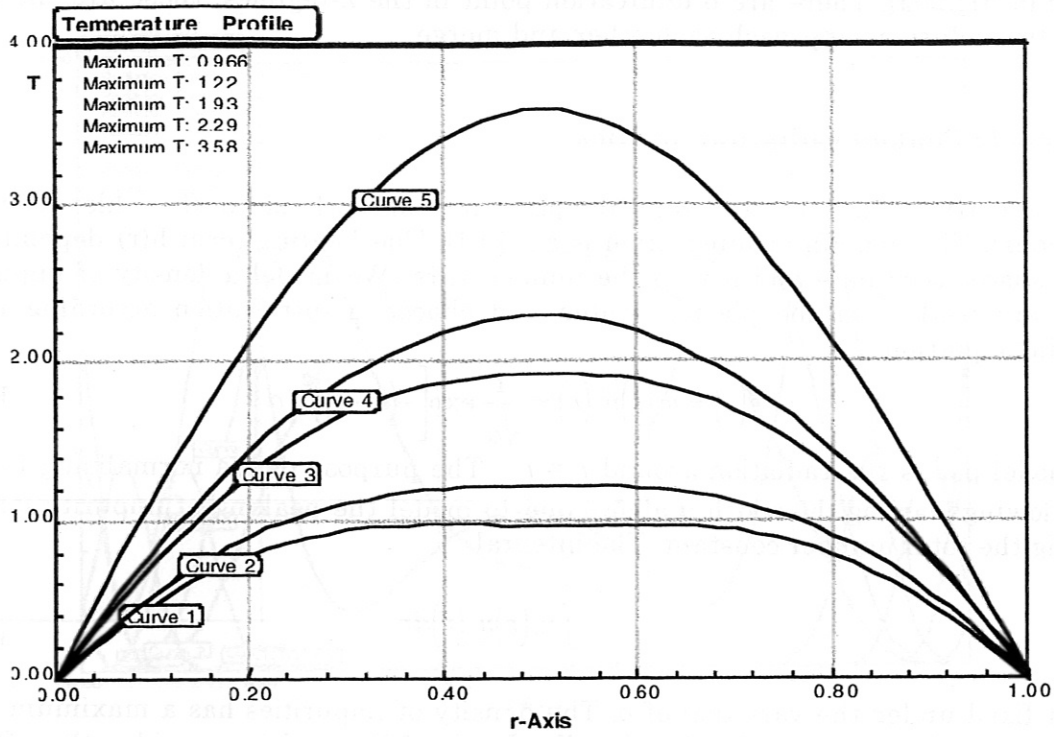

Fig. 22: Temperature profile of example 5. Peaked radiation profile, a = 0.05, r_1 = 0.5. Heating function: h_0 = 35, r_0 = 0.5, width w = 0.2. Radiation function 1: λ = 64, T_{max1}= 0.8, width w1 = 0.4. Radiation function 2: F = 0.3, T_{max2} = 2.0, width w2 = 0.1. Conductivity: χ = 1. Boundary conditions: eps = 0.0, xp = 2.333.

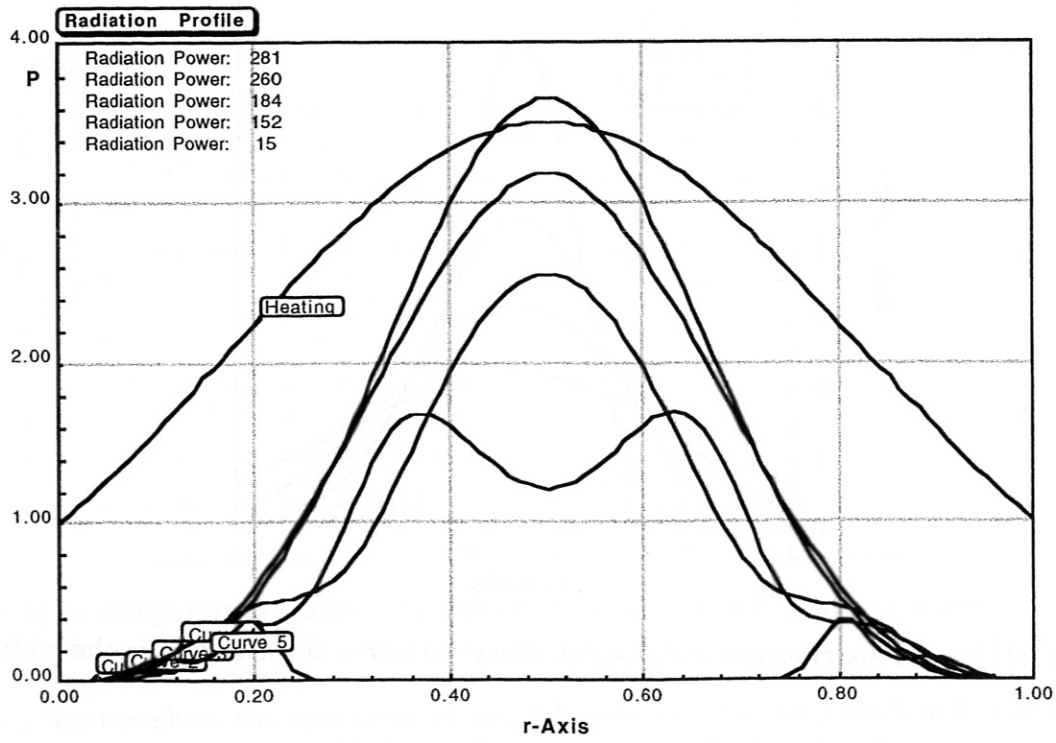

Fig. 23: Heating profile and radiation functions. Data as in Fig. 22

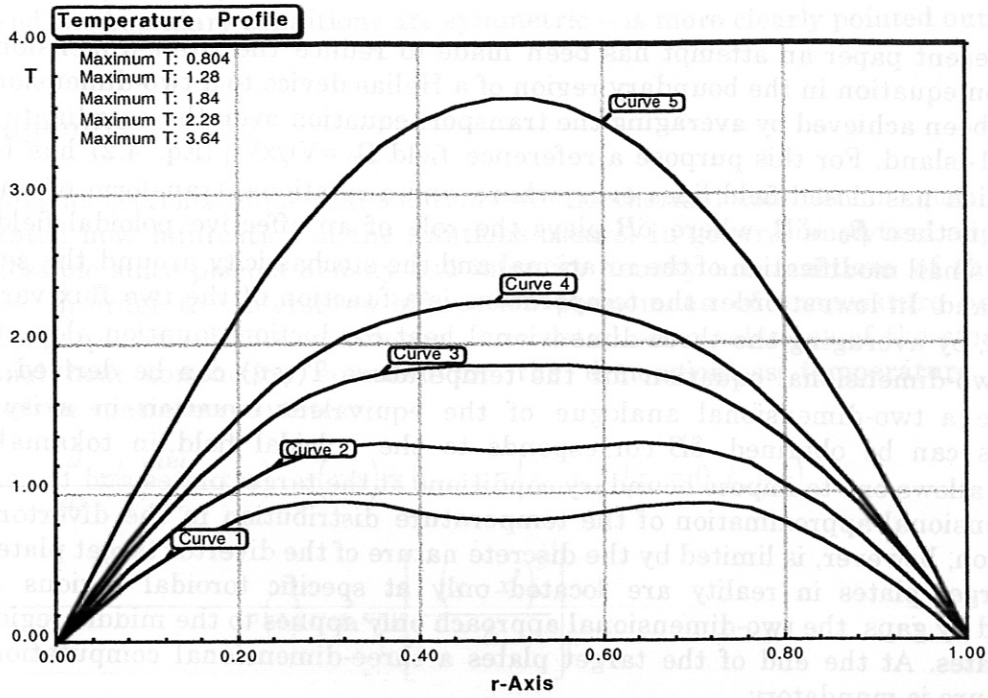

Fig. 24: Temperature profile of example 5. Peaked radiation profile, a = 0.02, r_1 = 0.5. Heating function: h_0 = 35, r_0 = 0.5, width w = 0.2. Radiation function 1: λ = 64, T_{max1}= 0.8, width w1 = 0.4. Radiation function 2: F = 0.3, T_{max2} = 2.0, width w2 = 0.1. Conductivity: χ = 1. Boundary conditions: eps = 0.0, xp = 2.333.

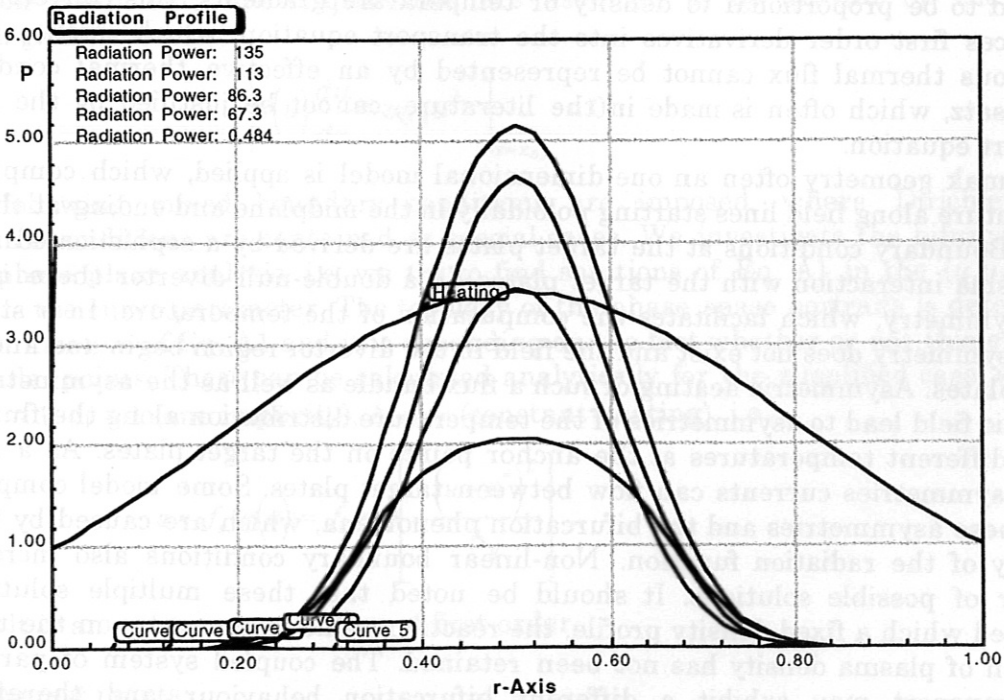

Fig. 25: Heating profile and radiation functions. Data as in Fig. 24

This example shows how a hollow temperature can arise if the radiation loss is larger than the heating power.

8. Conlusions

In the present paper an attempt has been made to reduce the three-dimensional heat conduction equation in the boundary region of a Helias device to a two-dimensional one. This has been achieved by averaging the transport equation over the coordinate parallel to the ι=1-island. For this purpose a reference field $\boldsymbol{B}_0 = \nabla\psi \times \nabla\eta$ (Eq. 4.2) has been defined, which has closed field lines everywhere and a rotational transform of unity. The real field is then $\boldsymbol{B}_0 + \delta\boldsymbol{B}$, where $\delta\boldsymbol{B}$ plays the role of an effective poloidal field, which creates a small modification of the rotational and the stochasticity around the separatrix of the island. In lowest order the temperature is a function of the two flux variables ψ an η, and, by averaging the three-dimensional heat conduction equation along the field lines a two-dimensional equation for the temperature $T(\psi,\eta)$ can be derived. By this procedure a two-dimensional analogue of the equivalent equation in axisymmetric tokamaks can be obtained. $\delta\boldsymbol{B}$ corresponds to the poloidal field in tokamaks. This equation allows one to impose boundary conditions at the target plates and to compute a two-dimensional approximation of the temperature distribution in the divertor region. Application, however, is limited by the discrete nature of the divertor target plates. Since these target plates in reality are located only at specific toroidal regions and are separated by gaps, the two-dimensional approach only applies to the middle region of the target plates. At the end of the target plates a three-dimensional computation of the temperature is mandatory.

Anomalous transport in the divertor region can lead to the beneficial effect of widening the outflow channel and thus reducing the power density on the target plates. Magnetic fluctuations have the same effect as the static poloidal field $\delta\boldsymbol{B}$: together with the large parallel heat conduction they generate an effective perpendicular thermal conductivity. Electric fluctuations, however, introduce a convective term $\langle\delta n \delta v\rangle \nabla T$, where $\langle\delta n \delta v\rangle$ is the anomalous particle flux density in the divertor region. Even if the particle flux is assumed to be proportional to density or temperature gradients, this convective term introduces first order derivatives into the transport equation, which implies that the anomalous thermal flux cannot be represented by an effective thermal conductivity. This ansatz, which often is made in the literature, cannot be justified by the rigorous transport equation.

In tokamak geometry often an one-dimensional model is applied, which computes the temperature along field lines starting poloidally in the midplane and ending at the target plates. Boundary conditions at the target plates are derived by a sophisticated model of the plasma interaction with the target plates. In a double-null divertor there is an up-down symmetry, which facilitates the computation of the temperature. In a stellarator such a symmetry does not exist and the field in the divertor region begin and and end on target plates. Asymmetric heating of such a flux bundle as well as the asymmetry of the magnetic field lead to asymmetries of the temperature distribution along the flux bundle and to different temperatures at the anchor points on the target plates. As a result of these asymmetries currents can flow between target plates. Some model computations show these asymmetries and the bifurcation phenomena, which are caused by the non-linearity of the radiation function. Non-linear boundary conditions also increase the number of possible solutions. It should be noted that these multiple solutions are computed which a fixed density profile, the reaction of the temperature on the transport equation of plasma density has not been retained. The coupled system of particle and heat transport may exhibit a different bifurcation behaviour and therefore the computations presented above are only a part of the truth, however, it must be expected, that the boundary condition do not uniquely determine the temperature distribution in the divertor region. The analytical model discussed in the appendix illustrates the various bifurcation events and helps to gain a better understanding of the

numerical examples. In particular, the occurence of asymmetric profiles – even if the heating and the boundary conditions are symmetric – is more clearly pointed out.

9. Appendix

In the previous sections numerical solutions of the thermal conduction equation have demonstrated how bifurcation of the solutions occurs. In general analytical approaches are not possible since plasma density and impurity density are functions of the spatial coordinate. In order to understand bifurcation phenomena of temperature profiles in radiative edge plasmas let us consider in more detail some solutions of the steady one-dimensional heat conduction equation for the dimensionless temperature u as a function of the spatial coordinate x

$$\frac{d}{dx}\kappa(u)\frac{du}{dx} + s(x) - q(x,u) = 0 \quad , \quad x \in [x_0, x_n] \quad (x_0 = 0, x_n = 1) \quad , \qquad \text{Eq. A 1}$$

$$s(x) := f_s \exp\left[-\frac{(x - x^*)^2}{\Delta_s}\right], \qquad \text{Eq. A 2}$$

$$q(x,u) := f_q \sum_{m=1}^{M} c_m(x) \exp\left[-\frac{(u - u_m^*)^2}{\Delta_{qm}}\right] \quad ; \quad \kappa(u) := \kappa_0 u^{\delta} \quad . \qquad \text{Eq. A 3}$$

s - heating term, q - radiation loss function (M - number of impurities), κ - heat conduction coefficient. These quantities are assumed to be defined by the model functions given above.

$$\left|\kappa(u)\frac{du}{dx} \mp \alpha_{0,n} u^{\beta_{0,n}}\right|_{x=x_{0,n}} = 0 \quad . \qquad \text{Eq. A 4}$$

In the following mixed boundary conditions are imposed, where Dirichlet's and Neumann's conditions are contained as special cases. We investigate the bifurcation by using a phase plane analysis, i.e. we try to find solutions of Eq. A1 in the (u,u_x)-plane where x is the curve parameter. The topology of the phase space portraits is determined by the parameters of Eq. A1 and it is depending on the fact whether or not this equation has singular points. These can be calculated analytically for the simplified case: $\kappa = \kappa_0 =$ const, $M = 1$, $c_1 = 1$ (one impurity), $\Delta_s \to \infty$ (constant heating), i.e.

$$s = f_s, \; q(u) := f_q \exp\left[-\frac{(u - u^*)^2}{\Delta_q}\right]. \qquad \text{Eq. A 5}$$

The result is an autonomous system of first-order.
Result:
$f_s > f_q$ – no rest points
$f_s < f_q$ – 2 rest points $P_{1,2}$ ($P:=(u,u_x)$ - phase plane point) with the eigenvalues $\lambda^{(1,2)}$ (calculated in a linearized approach)
P1 (Saddle):

$$u_1 = u^* - \sqrt{\Delta_q \ln \frac{f_q}{f_s}},\ u_{x1} = 0,\ \lambda_{1,2}^{(1)} = \pm \sqrt{\frac{1}{\kappa_0} \frac{2f_s}{\sqrt{\Delta_q}} \ln \frac{f_q}{f_s}}\ . \qquad \text{Eq. A 6}$$

P2(Vortex):

$$u_2 = u^* - \sqrt{\Delta_q \ln \frac{f_q}{f_s}},\ u_{x2} = 0,\ \lambda_{1,2}^{(1)} = \pm i \sqrt{\frac{1}{\kappa_0} \frac{2f_s}{\sqrt{\Delta_q}} \ln \frac{f_q}{f_s}}\ . \qquad \text{Eq. A 7}$$

Thus, for $f_s < f_q$ we have an island structure, for $f_s > f_q$ we have not. Hence, the equation $f_s = q_{max} = f_q$ defines a bifurcation point in the control space. This result can easily be generalized for the case of several impurities M > 1 (M = 2 see below) where chains of M saddle/vortex may appear.

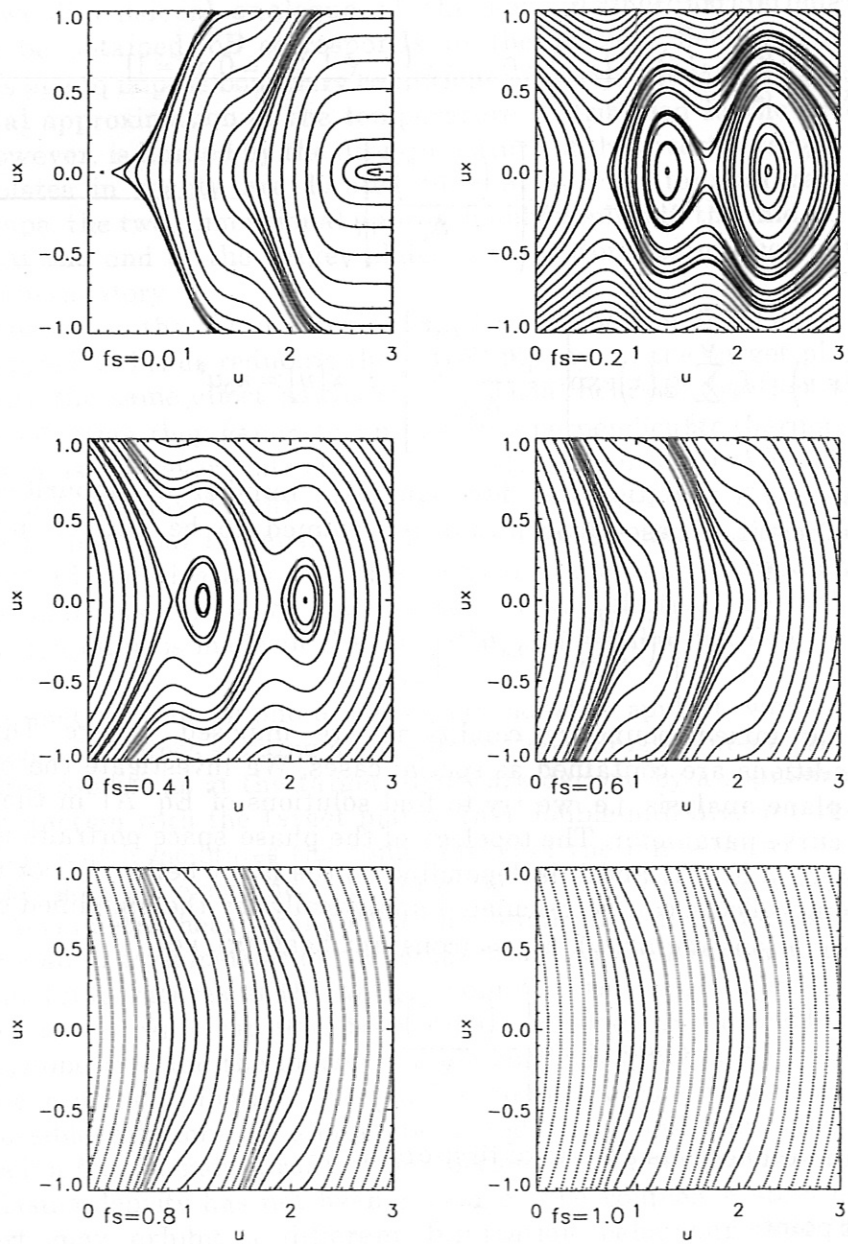

Fig. A 1: Phase plane portraits (u, u_x) for f_s as control parameter and Eq. A9

Let us consider the example E1:

$$\kappa = \kappa_0 = \frac{1}{2},\ M = 2,\ c_1 = c_2 = \frac{1}{2}, f_q = 1,\ u_1^* = 1, u_2^* = 2,\ \Delta_{q,1,2} = 0.1 \qquad \text{Eq. A 8}$$

If we assume the solutions $u(x,f_s)$ bounded on $[-\infty,\infty]$ they have at least one maximum, say at $x = x_m$ where $u = u_m$, $u_x = 0$. Let us start there and solve this initial value problem for $x \to \pm\infty$ for $u_m \in (0,\infty)$. Thus, we obtain all possible solutions and their resp. phase plane trajectories, depicted in Fig. A1, which have a bifurcation point at $f_s = q_{max} = 1/2$. Hence, we can decide whether or not boundary value problems with conditions (Eq.A5) are solvable. E.g., we can answer the question how many u_{max} exist for one parameter set (hysteresis) and how bifurcation occurs. The boundary conditions (Eq.A5) as relations between temperature u and its gradient u_x at the boundary points of the domain $[x_0,x_n]$ represent curves in the phase plane. If one phase plane trajectory starts with $x = x_0$ at the first boundary curve and attains the other one at $x = x_n$ this proves the respective $u(x)$ to be one solution of the boundary value problem under consideration.

Let us consider the two kinds of phase plane trajectories, i.e. (i) no rest points (no islands) and (ii) rest points (islands), and assume the boundary value curves to be well behaved. (i) The phase plane trajectories are monotonic above and below the u-axis. Then each boundary value curve crosses one phase plane trajectory only once. If these intersection points belong to the boundary points, one has one solution. Multiple solutions are possible (hysteresis; see Figs. A2, A3).

Example E2: Boundary value problem,

$$\alpha_{0,n} = 4,\ \beta_{0,n} = \frac{1}{2}, \qquad \text{Eq. A 9}$$

$$\kappa = \frac{1}{2},\ M = 2,\ c_1 = 1, c_2 = \frac{1}{2}, f_q = 9,\ u_1^* = 1, u_2^* = 2,\ \Delta_{q,1,2} = 0.1 \qquad \text{Eq. A 10}$$

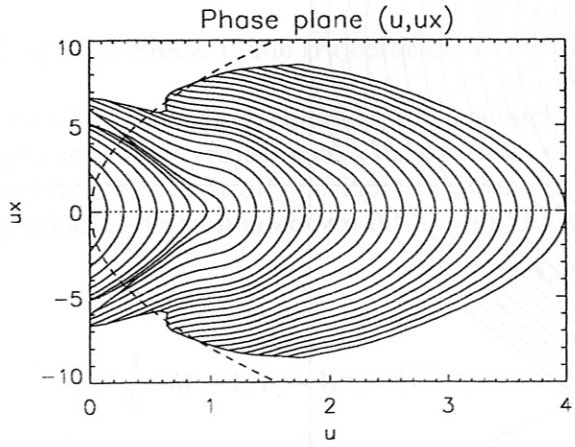

Fig. A 2: Phase plane trajectories together with the boundary values curves (dashed) for E2.

Fig. A2 shows phase plane trajectories for x = 0-1, x_m = 0.5) together with the boundary value curves. Each of them has 5 intersection points, i.e. there are 5 solutions to the boundary value problem which are represented together with the radiation profiles in Figs. 3

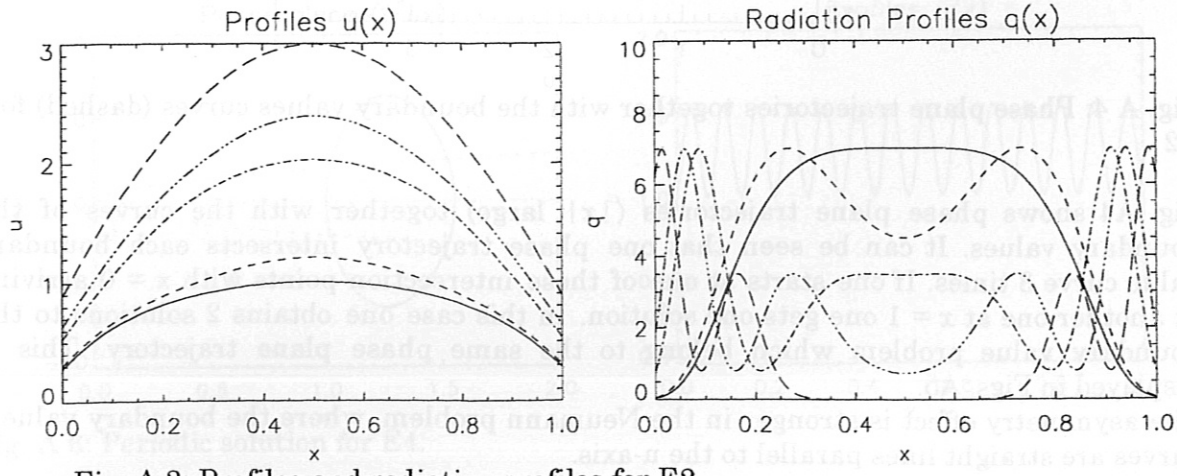

Fig. A 3: Profiles and radiation profiles for E2.

(ii) The appearance of the islands destroys the monotonicity and changes the phase plane trajectories such that one boundary value curve intersects one phase space trajectory several times. The results is that different profiles belong to the same phase plane trajectory. Asymmetric solutions to an otherwise symmetric problem may appear [13] (See also Fig. 11). The reason for this is the appearance of island structures in the phase plane.

Example E3: Boundary value problem,

$$\alpha_{0,n} = 2.947,\ \beta_{0,n} = 0.429 \quad , \qquad \text{Eq. A 11}$$

$$\kappa = \frac{1}{2},\ M = 1,\ c_1 = 1, f_s = 8, f_q = 20,\ u_1^* = 1, u_2^* = 2,\ \Delta_{q,1,2} = 0.1 \quad . \qquad \text{Eq. A 12}$$

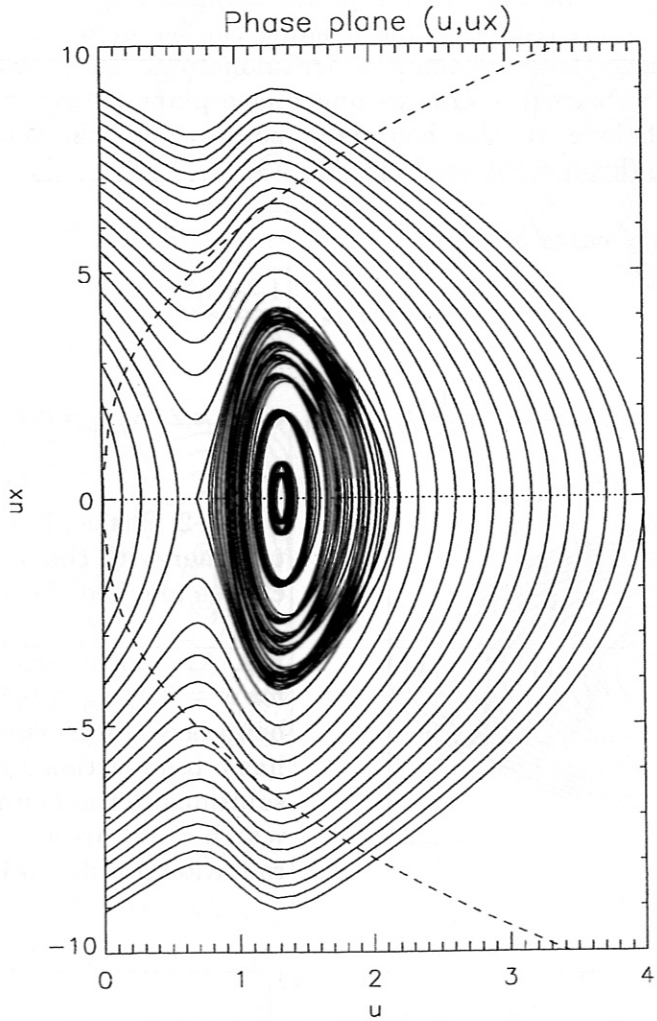

Fig. A 4: Phase plane trajectories together with the boundary values curves (dashed) for E2

Fig. A4 shows phase plane trajectories ($|x|$ large) together with the curves of the boundary values. It can be seen that one phase trajectory intersects each boundary value curve 3 times. If one starts at one of these intersection points with x = 0 arriving at another one at x = 1 one gets one solution. In this case one obtains 2 solutions to the boundary value problem which belong to the same phase plane trajectory. This is displayed in Figs. A5.
The asymmetry effect is stronger in the Neumann problem, where the boundary value curves are straight lines parallel to the u-axis.

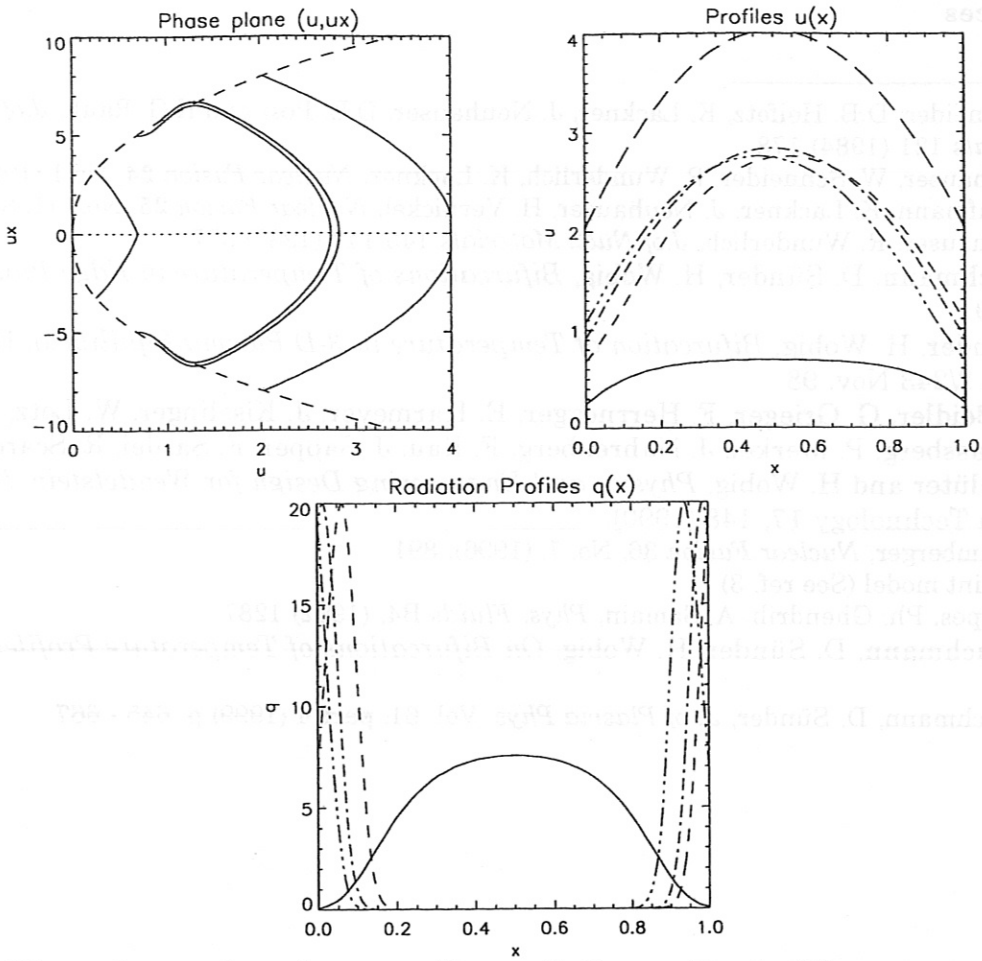

Fig. A 5: Phase plane trajectories, u–profiles, radiation profiles for E3.

(ii') The boundary value curves are such that they penetrate islands and intersect closed phase space trajectories. In addition to the types of solution mentioned above the existence of spatially periodic solutions is possible. This can be seen in Fig. A6 where one periodic solution is shown for example E4:

$$\alpha_{0,n} = 4,\ \beta_{0,n} = 0.5 \quad , \qquad \text{Eq. A 13}$$

$$\kappa = \frac{1}{2},\ M = 1,\ c_1 = 1, f_s = 10^3, f_q = 2\times 10^3,\ u_1^* = 1,\ \Delta_{q,1,2} = 0.1 \quad . \qquad \text{Eq. A 14}$$

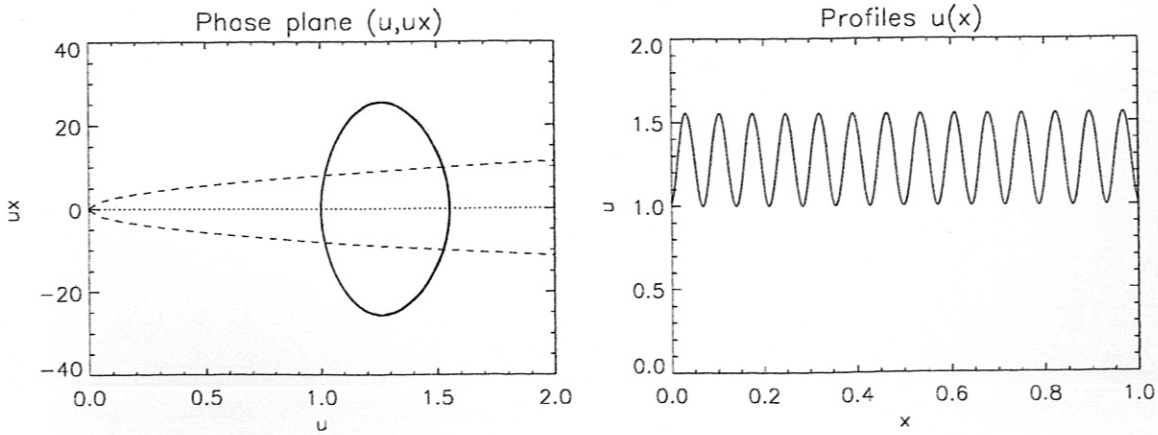

Fig. A 6: Periodic solution for E4.

References

[1] W. Schneider, D.B. Heifetz, K. Lackner, J. Neuhauser, D.E. Post and K.G. Rauh, *J.of Nucl. Materials* 121 (1984) 178

[2] J. Neuhauser, W. Schneider, R. Wunderlich, K. Lackner, *Nuclear Fusion* **24**, No.1 (1984) 39

[3] M. Kaufmann, K. Lackner, J. Neuhauser, H. Vernickel, *Nuclear Fusion* **25**, No.1 (1985) 89

[4] J. Neuhauser, R. Wunderlich, *J.of Nucl. Materials* 145-147 (1987) 877

[5] P. Bachmann, D. Sünder, H. Wobig, *Bifurcations of Temperature in Edge Plasmas*, PET 99

[6] D. Sünder, H. Wobig, *Bifurcation of Temperature in 3-D Plasma Equilibria*, IPP Report 2/243 Nov. 98

[7] C.D. Beidler, G. Grieger, F. Herrnegger, E. Harmeyer, J. Kisslinger, W. Lotz, H. Maassberg, P. Merkel, J. Nührenberg, F. Rau, J. Sapper, F. Sardei, R. Scardovelli, A. Schlüter and H. Wobig, *Physics and Engineering Design for Wendelstein 7-X,* Fusion Technology **17**, 148 (1990).

[8] E. Strumberger, *Nuclear Fusion* 36, No. 7, (1996), 891

[9] Twopoint model (See ref. 3)

[10] H. Capes, Ph. Ghendrih, A. Samain, *Phys. Fluids* B4, (1992) 1287

[11] P. Bachmann, D. Sünder, H. Wobig, *On Bifurcations of Temperature Profiles*, PET 97

[12] P. Bachmann, D. Sünder, *J. of Plasma Phys.* Vol. 61, part 4 (1999) p. 645 - 667